Marine and Petroleum Geology 163 (2024) 106760

Contents lists available at ScienceDirect

Marine and Petroleum Geology

journal homepage: www.elsevier.com/locate/marpetgeo

Paleoenvironmental reconstruction of the Berriasian organic-rich interval of the Vaca Muerta Formation (Neuquén Basin, Argentina): Insights for the characterization of unconventional hydrocarbon shale reservoirs

Ignacio A. Capelli [a,b,*], Roberto A. Scasso [a,b], Jorge E. Spangenberg [c], Diego A. Kietzmann [a,b], Mercedes Prámparo [d], Thierry Adatte [e]

[a] *Universidad de Buenos Aires, Facultad de Ciencias Exactas y Naturales, Departamento de Ciencias Geológicas, Intendente Güiraldes 2160 (CP 1428), Ciudad Autónoma de Buenos Aires, Argentina*
[b] *CONICET-Universidad de Buenos Aires. Instituto de Geociencias Básicas, Aplicadas y Ambientales de Buenos Aires (IGeBA), Intendente Güiraldes 2160 (CP 1428), Ciudad Autónoma de Buenos Aires, Argentina*
[c] *Institut des Dynamiques de la Surface Terrestre (IDYST), Université de Lausanne, Quartier UNIL-Mouline, Bâtiment Géopolis (CH 1015), Lausanne, Switzerland*
[d] *CONICET, Instituto Argentino de Nivología, Glaciología y Ciencias Ambientales (IANIGLA), Av. A. Ruiz Leal s/n (CP 5500) Mendoza, Argentina*
[e] *Institut des Sciences de la Terre (ISTE), Université de Lausanne, Quartier UNIL-Mouline, Bâtiment Géopolis (CH 1015), Lausanne, Switzerland*

A R T I C L E I N F O

Keywords:
Mineralogy
Trace elements
Organic matter
Palynology
Diagenesis
Stable isotopes -Vaca Muerta Fm

A B S T R A C T

The 50 m-thick Berriasian organic-rich interval (BORI) of the Vaca Muerta Formation (Neuquén Basin, Argentina) represents one of the most attractive stratigraphic intervals for unconventional hydrocarbon exploration in the unit. Nevertheless, little is known about the environmental conditions prevailing during the accumulation of the sediments. To unravel the causes that favored the preservation of the organic matter (OM) in the BORI, a detailed multiproxy sedimentological approach was conducted. The study included the analyses of microfacies, palynological content, calpionellid-calcisphere dinocysts, mineralogy, spectral gamma-ray, inorganic geochemistry, Rock-Eval pyrolysis and stable carbon isotopes of whole rock carbonate ($\delta^{13}C_{carb}$), and associated OM ($\delta^{13}C_{org}$). The BORI presents a late Early to early Late Berriasian age and is subdivided into a lower and upper interval. The lower interval (25.6 m-thick) is primarily formed by radiolaritic wackestones and presents higher total organic carbon (TOC) content (4.2 wt% on average), mainly in the form of amorphous OM (AOM), with variable contribution of phytoclasts. The geochemical analyses (Si, Ni, Cu, Mo, U, V) indicate high productivity of the water column and overall sea bottom anoxia. Oppositely, the upper interval (24.4 m-thick) is mostly constituted by peloidal packstones/grainstones and presents a lower TOC content (1.5 wt% on average) mainly constituted by phytoclasts, with variable contribution of AOM. A decrease of the productivity and an increase of sea bottom oxygenation is recorded based on the geochemical analyses. The high OM content of the BORI responds to the combination of high productivity of the water column and sea bottom anoxia in response to the Berriasian transgression and a worldwide paleoclimatic change towards more humid conditions. The results of our study position the BORI as an attractive interval for unconventional hydrocarbon production due to its high TOC, low bulk clay mineral and high biogenic quartz content, granting an adequate geomechanical behavior.

1. Introduction

The Vaca Muerta Formation (VMFm) is an organic and carbonate-rich marine shale unit deposited during the Late Jurassic-Early Cretaceous in the Neuquén Basin, western Argentina. The VMFm has received worldwide attention during the last decade since it is regarded as the first economical unconventional hydrocarbon play outside the United States (Minisini et al., 2020a). The key factors explaining the success of the VMFm as an unconventional hydrocarbon play are the high total organic carbon (TOC) content (up to 12 wt%), the wide geographical

* Corresponding author. Universidad de Buenos Aires, Facultad de Ciencias Exactas y Naturales, Departamento de Ciencias Geológicas, Intendente Güiraldes 2160 (CP 1428), Ciudad Autónoma de Buenos Aires, Argentina.
E-mail address: capelli@gl.fcen.uba.ar (I.A. Capelli).

https://doi.org/10.1016/j.marpetgeo.2024.106760
Received 24 June 2023; Received in revised form 7 February 2024; Accepted 12 February 2024
Available online 20 February 2024
0264-8172/

distribution (about 30,000 km^2), the great thickness (up to 700 m), the broad range of maturity (vitrinite R_o 0.8–3%) of the organic matter (OM), and a clay mineral content lower than 40 wt% that grants adequate brittleness to conduct appropriate hydraulic fracturing (Leanza and Hugo, 1977; Askenazi et al., 2013; Stinco and Barredo, 2014; Legarreta and Villar, 2015; Kietzmann et al., 2016; Minisini et al., 2020a; Brisson et al., 2020; Capelli et al., 2020; Veiga et al., 2020). The abundant and excellent surface exposures of the unit favored detailed sedimentological and stratigraphic observations for understanding the genesis and distribution of the VMFm basinwide (Weaver, 1931; Leanza and Hugo, 1977; Mitchum and Uliana, 1985; Legarreta and Gulisano, 1989; Scasso et al., 2002, 2005; Spalletti et al., 2014, 2015; Kietzmann et al., 2014, 2016, 2020, 2021a, 2023; Paz et al., 2022).

Despite the great thickness of the VMFm, only specific stratigraphic intervals are the main targets for the unconventional hydrocarbon production of the unit (e.g., Spalletti et al., 2014, 2015; Desjardins et al., 2016; Domínguez et al., 2016, 2020; Lanusse Noguera et al., 2017; de Barrio et al., 2018). These intervals are characterized by high TOC content (2–12 wt%), total porosity (~13%) and hydrocarbon saturation (~0.4–0.8), and their stratigraphic distribution is the result of paleoenvironmental conditions mostly driven by a combination of eustatism and tectonism (Kietzmann et al., 2014, 2016; Spalletti et al., 2015; Domínguez et al., 2016, 2020; Veiga et al., 2018, 2020). One of those organic-rich intervals in the VMFm is a ~50 m-thick marly succession of Late Berriasian age, referred in the oil-industry as "*segunda cocina*" (second kitchen) (Desjardins et al., 2016; Domínguez et al., 2016, 2020). This interval is an attractive target in the NW part of the basin, where the combination of a high TOC content and proper petrophysical and geomechanical features may enable unconventional hydrocarbon production (Fantin et al., 2014; Crousse et al., 2015; Lanusse Noguera et al., 2017; de Barrio et al., 2018). Despite the huge economic importance of this interval, the paleoenvironmental conditions that favored the accumulation and preservation of the OM in this specific interval have not been previously studied.

It is generally assumed that the OM of the VMFm is composed mostly by unstructured material formed through the transformation of algae (Brisson et al., 2020). The OM was accumulated in a low-energy, distal setting within a low gradient carbonate ramp, characterized by high productivity of the water column and overall oxygen-depleted sea bottom conditions which favored the preservation of the OM (Scasso et al., 2005; Kietzmann et al., 2014; Spalletti et al., 2014; Krim et al., 2017, 2019; Capelli et al., 2018, 2020; Rodriguez Blanco et al., 2018; Brisson et al., 2020; Minisini et al., 2020b). In addition to the poorly oxygenated sea bottom, the relatively high sedimentation rate associated with muddy hyperpycnal flows may have also contributed to a quick overburden, thus favoring the preservation of the OM (Otharán et al., 2020; Minisini et al., 2020b).

Previous mineralogical and geochemical studies have shown that the composition of the marls and limestones of the VMFm responds to multiple and independent variables, including the provenance of the sediment (Scasso et al., 2002; Spalletti et al., 2014, 2015; Krim et al., 2017, 2019; Milliken et al., 2019; Rodriguez Blanco et al., 2020; Capelli, 2021; Otharán et al., 2022), the productivity of the water column (Milliken et al., 2019; Capelli et al., 2020; Otharán et al., 2022; Musacchio et al., 2022), the sea level changes (Kietzmann et al., 2014, 2016; Zeller et al., 2015), the paleoclimate in the hinterlands (Krim et al., 2017, 2019; Capelli et al., 2020; Paz et al., 2022), and the diagenetic grade reached by the unit in each studied section (Scasso et al., 2002, 2005; Catalano et al., 2018; Milliken et al., 2019; Capelli et al., 2020, 2021). Considering the complexity of the sedimentary environment, the reconstruction of the environmental conditions of accumulation and preservation of the OM for VMFm is a challenging aim, only attainable by working with detailed multiproxy analyses.

Paleoenvironmental reconstructions in the VMFm were conducted on the basis of inorganic geochemical studies (e.g., Scasso et al., 2002, 2005; Spalletti et al., 2014, 2015, 2019; Rodriguez Blanco et al., 2018; Gómez Dacal et al., 2018) and detailed sedimentological analyses which often included the study of trace fossils (e.g., Spalletti et al., 2000; Scasso et al., 2002, 2005; Kietzmann et al., 2014, 2016; Otharán et al., 2020; 2022; Paz et al., 2021, 2022, 2023). These studies consisted either in broad paleoenvironmental reconstructions of the entire VMFm (Krim et al., 2017, 2019; Capelli et al., 2018, 2020; Spalletti et al., 2019) or in detailed paleoenvironmental analysis of specific Tithonian intervals (Scasso et al., 2002, 2005; Spalletti et al., 2014, 2015; Ravier et al., 2020; Paz et al., 2021), but none of them were focused in the study of the environmental conditions that favored the accumulation and preservation of the OM in the Berriasian Organic-Rich Interval (BORI) of the VMFm. Furthermore, no previous studies combining the petrography, palynology, mineralogy, biostratigraphy and geochemistry of both bulk rock and OM were conducted in the VMFm.

This paper examines in detail for the first time the petrography, mineralogy, and inorganic geochemistry of the BORI of the VMFm in Puerta Curaco section (northern Neuquén Province, Argentina) including biostratigraphic (calpionellids and calcisphere dinocysts) and palynofacies analysis together with the determination of the amount, type, maturation and carbon stable isotope composition of OM. This detailed multiproxy sedimentological approach was done with a threefold objective: 1) characterize the mineralogy and geochemistry of the BORI and their changes throughout the interval, 2) reconstruct the paleoenvironmental conditions during the accumulation of the organic-rich deposits, and 3) discuss how the mineralogical and geochemical trends may affect the reservoir quality. The results are useful for comparison with subsurface successions of hydrocarbon-bearing blocks, where the BORI of the VMFm is considered as a potential stratigraphic interval for unconventional hydrocarbon production.

2. Geological setting and tectonic evolution of the Neuquén Basin

The Neuquén Basin is a prolific hydrocarbon basin located in the western part of Argentina (Uliana and Legarreta, 1993; Vergani et al., 1995; Legarreta and Villar, 2015; Veiga et al., 2020). The basin was originated in response to a rift process that occurred in the western margin of Gondwana between the Late Triassic and the Early Jurassic. The extensional regime generated a series of isolated depocenters which were filled by siliciclastic and volcaniclastic continental deposits (Gulisano, 1981; Vergani et al., 1995). From the Early Jurassic to the Late Cretaceous, the basin underwent a post-rift stage and strong thermal subsidence. Multiple paleo-Pacific marine transgressions occurred, filling the basin with a varied marine and continental succession (Mitchum and Uliana, 1985; Legarreta and Gulisano, 1989), and a volcanic-arc complex developed along the western margin of the basin in response to the proto-Pacific plate subduction (Legarreta and Uliana, 1991). In this framework, the organic-rich deposits of the VMFm were accumulated during the Tithonian transgression (Mitchum and Uliana, 1985; Legarreta and Gulisano, 1989; Spalletti et al., 2000; Scasso et al., 2002; Kietzmann et al., 2014). Later, during the Late Cretaceous to Cenozoic, the compressive regime of the Andean Orogeny resulted in a fold and thrust belt with an associated foreland basin to the east. The Neuquén Basin was fully disconnected from the paleo-Pacific Ocean and sedimentation was mostly constituted by terrestrial deposits (Legarreta and Gulisano, 1989; Ramos, 1999; Howell et al., 2005).

2.1. *Sequence stratigraphy of the Vaca Muerta Formation: origin of the Berriasian organic-rich interval*

Several sequence-stratigraphic schemes mostly based on the recognition of flooding surfaces and stacking patterns were proposed for the Late Jurassic-Early Cretaceous VMFm (Spalletti et al., 2000; Kietzmann et al., 2014, 2016; Zeller et al., 2015; Desjardins et al., 2016; Domínguez et al., 2020). Some of them were achieved by combining subsurface seismic stratigraphy with outcrop sedimentary facies analyses (Mitchum and Uliana, 1985; Legarreta and Gulisano, 1989; Kietzmann et al., 2014, 2016; Zeller et al., 2015; Legarreta and Villar, 2015; Desjardins et al., 2016; Domínguez et al., 2020; Reijenstein et al., 2020). The Lower Tithonian and the Upper Berriasian highstands produced two key organic-rich stratigraphic intervals, formed in response to paleo-Pacific marine transgressions (Spalletti et al., 2014, 2015; Kietzmann et al., 2014, 2021a; Desjardins et al., 2016; Domínguez et al., 2016, 2020).

The Lower Tithonian interval directly overlies the continental Tordillo Fm (Leanza and Hugo, 1977; Mitchum and Uliana, 1985; Legarreta and Gulisano, 1989) and presents a wide distribution throughout the basin (Domínguez et al., 2016, 2020, Fig. 1A). It is the result of a large marine transgression that deposited up to 60 m of organic-rich mudstones considered as the main organic-rich stratigraphic interval for hydrocarbon production in the VMFm due to its high TOC content (2–12 wt%) and porosity (e.g., Spalletti et al., 2014, 2015; Fantin et al., 2014; Desjardins et al., 2016; Domínguez et al., 2016, 2020; Lanusse Noguera et al., 2017). This stratigraphic interval is informally referred as "*cocina*" (kitchen) in the sequence stratigraphic framework of the VMFm (Desjardins et al., 2016; Domínguez et al., 2020; Minisini et al., 2020b).

Conversely, the distribution of the organic-rich deposits of the Berriasian transgression is restricted to the central part of the basin, since the accumulation of the BORI deposits were constrained by the Chihuidos Proto-high (also known as Cerro Arena paleo-high) (Domínguez et al., 2016, 2020; Micucci et al., 2018, Fig. 1A). This interval, known as "*segunda cocina*" (second kitchen) in the sequence stratigraphic framework of the VMFm (Domínguez et al., 2020), have demonstrated interesting petrophysical and geomechanical features in the Narambuena (Lanusse Noguera et al., 2017), El Trapial (Fantin et al., 2014; Crousse et al., 2015) and Chihuido de la Sierra Negra (Ponce et al., 2022) blocks, located approximately 70 km to the east of Puerta Curaco section (Fig. 1A).

2.2. The Vaca Muerta Formation in Puerta Curaco section

The Puerta Curaco section is located 30 km to the east of Chos Malal Town, in the north part of the Neuquén Province (Fig. 1A). There, the VMFm is formed by a 407 m-thick rhythmic succession of marls and limestones, with commonly interbedded microbial bindstones, calcite concretions, ash beds, and calcite beef-veins (Kietzmann et al., 2016, 2018a; Capelli et al., 2018, 2021; Rodriguez Blanco et al., 2018, 2022b;

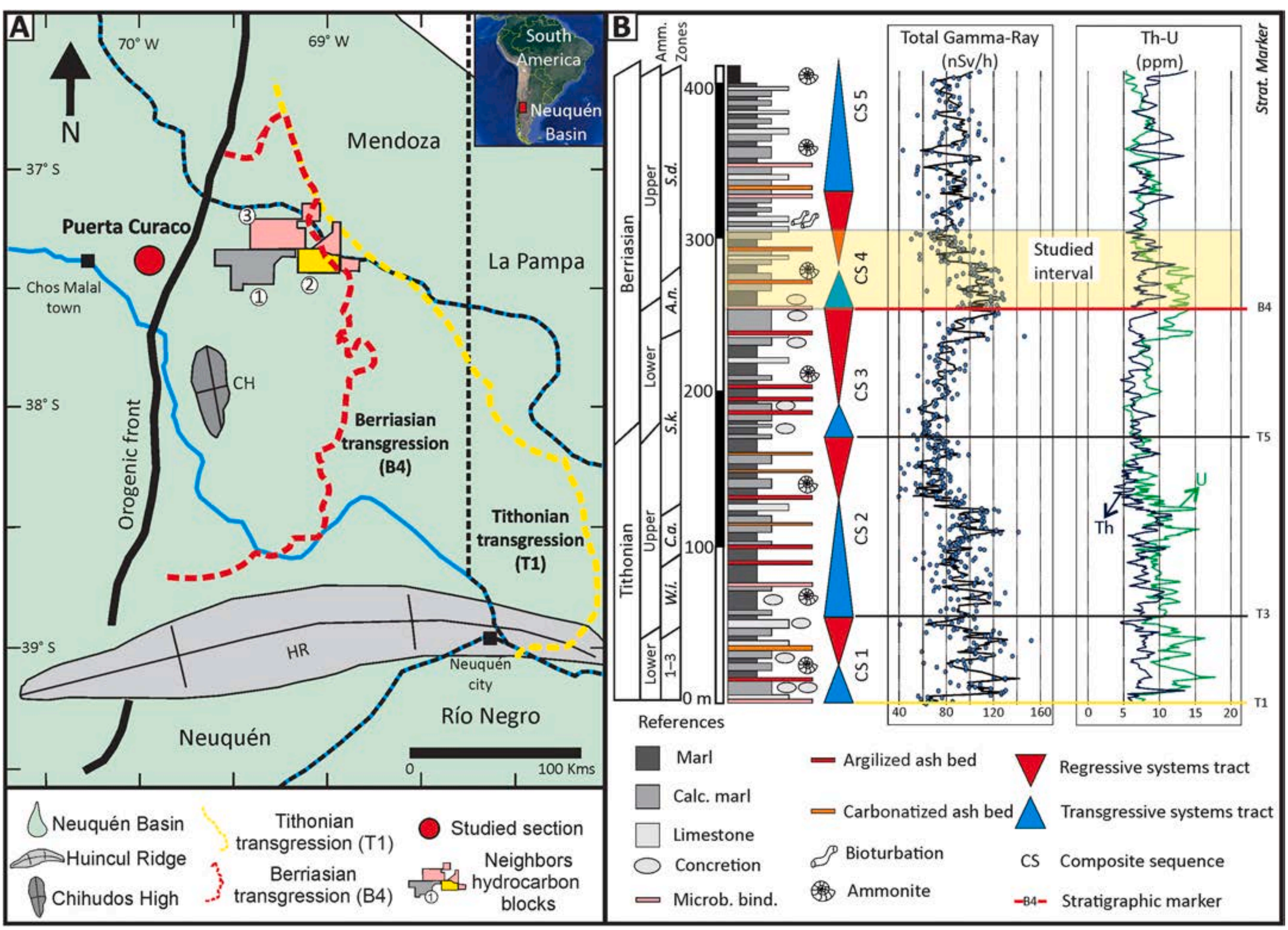

Fig. 1. **A)** Sketch map of the Neuquén Basin showing the location of the Puerta Curaco section, the orogenic front, and the two main structures of the basin: the Huincul Ridge (HR) and the Chihuidos Proto-High (CH). The yellow dashed line outlines the geographic distribution of the Lower Tithonian organic-rich deposits (thickness >10 m) and the red dashed line the distribution of the Berriasian organic-rich deposits (thickness >10 m) of the VMFm (modified from Domínguez et al., 2020). 1, 2 and 3 refer to El Trapial, Narambuena and Chihuido de la Sierra Negra oil blocks. **B**) Simplified litholog, ammonite zones, stratigraphic markers (T1, T3, T5, B4), and sequence stratigraphy scheme of the VMFm in Puerta Curaco section. The studied interval is marked in yellow and is included in the Composite Sequence 4, characterized by high Total Gamma-Ray and U values. Litholog, Total Gamma Ray, U and Th from Capelli et al. (2018). 1–3) *Virgatosphintes andesensis*, *Pseudolissoceras zitteli*, *Aulacosphintes proximus* ammonite Zones; W.i.) *Windhauseniceras internispinosum* ammonite Zone; C.a.) *Corongoceras alternans* ammonite Zone; S.k.) *Substeueroceras koeneni* ammonite Zone; A.n.) *Argentiniceras noduliferum* ammonite Zone; S.d.) *Spiticeras damesi* ammonite Zone; CS) Composite sequences (see Kietzmann et al., 2016). Stratigraphic markers (T1, T3, T5, B4) from Desjardins et al. (2016).

Weger et al., 2019, Fig. 1B) with an age spanning from the Early Tithonian to the Late Berriasian/Early Valanginian (Leanza and Hugo, 1977; Kietzmann et al., 2018a). The VMFm overlies the Tordillo Fm and is transitionally covered by the Quintuco Fm. Paleoenvironmental reconstructions indicate that VMFm sedimentation occurred in an outer carbonate ramp environment characterized by overall sea bottom anoxia and high sea water productivity (DÓdorico, 2009; Legarreta, 2009; Kietzmann et al., 2016; Capelli et al., 2018). Spectral Gamma Ray measurements show six intervals with high Total Gamma Ray values, all of them associated to high values of uranium and TOC (Weger et al., 2019; Weger and Eberli, 2017; Capelli et al., 2018; Tenaglia et al., 2020, Fig. 1B).

3. Materials and methods

3.1. Litholog and sampling

A 50 m-thick, bed-to-bed litholog was done in the BORI of the VMFm in Puerta Curaco section (Fig. 1A). The base of the studied interval is at 254.2 m from the base of the VMFm and its age spans from the late Early Berriasian to the early Late Berriasian (upper part of *A. noduliferum* to lower part of *S. damesi* ammonite zones; Kietzmann et al., 2018a). It corresponds to the transgressive systems tract of the Composite Sequence 4 in Kietzmann et al. (2016), to the interval B4–V1 in Desjardins et al. (2016), to the "*Sección Enriquecida Superior*" in de Barrio et al. (2018) and to the OVM8 in Domínguez et al. (2020).

Thickness was measured using a Jacob's staff and ninety-seven samples of mudstone, marl, calcareous marl, and limestone were collected every 0.5 m to perform petrographic, mineralogical and geochemical analyses. Field test with a few drops of HCl 10% v/v showed no to very subtle reaction on mudstones, whereas marls/calcareous marls and limestones had a strong reaction. X-ray diffraction semiquantitative analyses indicated calcite content of less than 10 wt% in mudstones, between 10 and 50 wt% in marls, between 50 and 65 wt% in calcareous marls, and >65 wt% in limestones. In this contribution, only mudstones, marls and calcareous marls are analyzed.

3.2. Microfacies and calcareous microfossils

Microfacies were determined under a conventional petrographic microscope in thin sections stained with alizarin red and potassium ferricyanide to distinguish calcite from dolomite (Evamy, 1963; Dickson, 1965). Sixteen thin sections in the BORI (253–305 m) and five below the BORI (230–253 m) were studied for biostratigraphic purposes. Calcareous microfossils (calpionellids and calcareous dinoflagellate cysts) were searched using a petrographic microscope Leica DM 750 with attached digital camera. Taxonomic determinations were supported by the Leica Application Suite software for micrometric measurements. Biozonation follow criteria used by Kietzmann et al. (2021a, 2023) in the VMFm. Samples are stored in the Institute of Basic, Applied and Environmental Geosciences of Buenos Aires (IGeBA), Argentina under the catalogue numbers: 26.3.16_110, 26.3.16_112, 26.3.16_118, 26.3.16_120, 26.3.16_121, PS_540, 26.3.16_123, PS_546, 26.3.16_127, PS_558, PS_563, PS_570, 27.3.16_134, PS_579.5, PS_580, PS_585, PS_585.5, PS_592, 27.3.16_139, PS_599, 27.3.16_141.

3.3. Bulk and clay mineralogy

The bulk mineralogy of fifty-two samples of mudstones, marls and calcareous marls was determined by X-ray diffraction (XRD) using a Thermo Scientific ARL X-TRA Diffractometer with a CuKα (1.540562 Å) at the Institute of Earth Sciences of the University of Lausanne using a voltage of 45 kV, a tube current of 40 mA, a count time of 1 s/step and a step size of 0.02° 2θ. The bulk mineralogy was analyzed in the range from 1 to 65° 2θ and quantified following the Rietveld Refinement Method (Rietveld, 1969), using the BGMN database and the Profex 4.0.2 software (Doebelin and Kleeberg, 2015). The estimated standard deviations vary between 0.1 and 1.4 wt% whereas the Goodness of fit of the refinement between 1.1 and 1.6. To determine the relative brittleness of the BORI, a mineralogical brittleness index was calculated following the equation proposed by Jarvie et al. (2007):

$$\text{Brittle Index} = \text{Quartz}\,(\%) / [\text{Quartz}\,(\%) + \text{Carbonate}\,(\%) + \text{Clay minerals}\,(\%)]$$

The clay mineralogy of forty-four samples of mudstones, marls and calcareous marls was determined in the <2 μm and 2–16 μm size fraction in oriented aggregates of decarbonated samples (Kübler, 1987; Adatte et al., 1996). Preparations were made on glass slides and analyzed in a range from 1 to 30° 2θ. Two measurements were performed: air-dried (AD) and ethylene glycol solvated (EG) and the identification of the clay minerals was done based on the position of the basal reflections (Moore and Reynolds, 1997). In order to discriminate between kaolinite and chlorite, samples characterized by a basal reflection at 12.4–12.5° 2θ were heated (550 °C during 2 h; Moore and Reynolds, 1997). The relative intensity (% in cps) of the main peak of each clay mineral was determined in the EG sample and used to estimate vertical variations of the clay mineralogy (Adatte et al., 1996). In this method, clay minerals are given in relative percent abundance (%) and without correction factors (Adatte et al., 1996). The Reichweite (ordering type) of the mixed-layer illite/smectite was calculated after measuring the Δ2θ in the EG samples (Moore and Reynolds, 1997).

3.4. Spectral gamma-ray

Ninety individual measurements were done every ~0.5 m using a RS 230 GammaRay Spectrometer. Individual measurements lasted 120 s and results included Total Gamma-Ray (TGR, nSv/h), K (%), Th (ppm) and U (ppm). Each radioelement is determined with the following equation:

$$n_i = S_{iK}C_K + S_{iU}C_U + S_{iTh}C_{Th} + n_{iBG}$$

Where n represents the count rate in the energy window, S_i the sensitivity of the spectrometer for the detection of each radioelement (K, Th, U), C the concentration of the element and n_{iBG} the background count rate (IAEA, 2003).

3.5. Elemental geochemistry

Major and trace elements (ME and TE) concentrations were determined in fifty-two samples of mudstones, marls and calcareous marls by X-ray fluorescence (XRF) spectrometry using an XRF Phillips PW2400 spectrometer with Rh-Kα radiation and a power of 2400 W at the Institute of Earth Sciences of the University of Lausanne. For ME analyses, samples were calcined and loss on ignition (LOI) was calculated by gravimetry. ME concentrations were then determined on fused discs after mixing 1.2 g of calcined sample powder with lithium tetraborate ($Li_2B_4O_7$). TE analyses were done in pressed discs, after mixing 12 g of powdered sample with Hoechst-wax-c. Detection limits are 0.01 wt% for ME and 1–7 ppm for TE and analytical precision was tested using certified international standards (BHVO2, TS5-6, and NIMG).

TE concentrations were normalized to aluminum to avoid dilution phenomena caused by the presence of carbonate (Calvert and Pedersen, 1993; Tribovillard et al., 2006) and enrichment factors (EF) of TE were calculated to study paleoredox and paleoproductivity conditions (e.g., Tribovillard et al., 2006) using the following equation:

$$X_{EF} = (X/Al)_{sample} / (X/Al)_{BG}$$

Where X_{EF} is the EF of the element, $(X/Al)_{sample}$ the X/Al ratio of the sample, and X/Al_{BG} the X/Al ratio of the considered background which was the Average Shale (Wedepohl, 1971). Additionally, the non-detrital contribution of silica (Si_{excess}) was estimated using the following equation (Ross and Bustin, 2009; Dong et al., 2018):

$$Si_{excess} = Si_{sample} - (Al_{sample} * (Si/Al)_{BG})$$

Where the $(Si/Al)_{BG}$ is the Si/Al ratio of the considered background, which was the Average Shale (3.11, Wedepohl, 1971). In this paper, the values of Si_{excess} are used to show relative vertical variations throughout the studied interval and not as absolute values.

3.6. Total organic carbon, organic matter type and maturation

Fifty samples of mudstones, marls and calcareous marls were analyzed by Rock-Eval pyrolysis to determine the TOC content, the type of OM and its maturation (Espitalié et al., 1985). Measurements were done over crushed samples using a Rock-Eval 6 instrument (Behar et al., 2001) at the Institute of Earth Sciences of the University of Lausanne and using the IFP160000 as international standard. Results included TOC (wt%), hydrogen index (HI, mg HC/g TOC, HC for hydrocarbons), oxygen index (OI, mg CO_2/g TOC) and temperature of maximum HC yield (T_{max}, °C). HI, OI and T_{max} values were only considered in those samples (n = 28) with TOC ≥0.3 wt% and pyrolytic hydrocarbons (S_2) ≥0.2 mg HC/g TOC (e.g., Fantasia et al., 2018). Additionally, TOC content was determined in thirteen samples using a LECO C230CH Carbon Analyzer (GeoLab Sur, Argentina). The analytical precision is < 0.1 wt% for TOC, 10 mg HC/g TOC for HI, 10 mg CO_2/g TOC for OI, and 1.5 °C for T_{max}.

Rock-Eval data was used to calculate the original TOC content (TOC_o) using the empirical formula developed for the VMFm by Brisson et al. (2020):

$$TOC_o = (TOC_p - [S1*0.08333] - [TOC_p*HI_p*0.0008333]) / (1-[HI_o*0.0008333])$$

Where TOC_p and HI_p are the present values of TOC and HI respectively, which are obtained from the Rock-Eval analyses. The HI_o corresponds to the original HI of the VMFm, estimated in 680 mg HC/g TOC (Brisson et al., 2020). The TOC_o was only calculated in samples with S_2 ≥ 0.2 mg HC/g TOC (n = 28).

3.7. Carbon and oxygen stable isotopes

The carbon and oxygen stable isotope composition of the carbonate ($\delta^{13}C_{carb}$ and $\delta^{18}O_{carb}$ respectively) were determined in aliquots of forty-one powdered whole-rock samples of marls/calcareous marls ($CaCO_3$ >10 wt%) following Révész and Landwehr (2002) and using a Thermo Fisher Scientific (Bremen, Germany) Gas Bench II carbonate preparation device connected to a Delta Plus XL isotope ratio mass spectrometer at the Institute of Earth Surface Dynamics of the University of Lausanne (UNIL). Analytical precision (1 standard deviation, SD) was determined by replicated analyzes of the laboratory standards NBS-19 and Carrara marble and was not greater than ±0.05 ‰ for $\delta^{13}C_{carb}$ and ±0.1 ‰ for $\delta^{18}O_{carb}$.

The organic carbon stable isotope composition ($\delta^{13}C_{org}$) was determined in forty-three decarbonated (treatment with 10% HCl) samples of mudstones, marls and calcareous marls at the Institute of Earth Surface Dynamics of the University of Lausanne by flash combustion on an elemental analyzer (Carlo Erba 1108 EA) interface to an isotope ratio mass spectrometer (Thermo Fisher Scientific Delta V Plus) via a Conflo III interface under continuous helium flow (Spangenberg et al., 2006). The carbon and oxygen isotope composition were reported in the delta (δ) notation as variations of the molar ratio (R) of the heavy to light isotopes (e.g., $^{13}C/^{12}C$) relative to an international standard: $\delta = (R_{sample} - R_{standard})/R_{standard}$. For carbon and oxygen, the standard is Vienna Pee Dee Belemnite limestone (VPDB), and values are given as per mil (‰) vs. VPDB. The repeatability and intermediate precision of the EA/IRMS analyses were determined by the SD of separately replicated analyses of international reference materials and UNIL-inhouse standards (see details in Spangenberg and Zufferey, 2019), and was better than 0.1‰.

3.8. Palynological analyses

Twenty-six samples were processed for palynology using standard techniques of maceration in HF and HCl (Volkheimer and Melendi, 1976). The residues were sieved with a 10 μm filter and a first slide for OM analysis was mounted in glycerin jelly. All the samples are stored in the palaeopalynological collection of the Unit of Paleopalynology, Argentinean Institute of Snow Research, Glaciology and Environmental Sciences (IANIGLA) Mendoza, Argentina, under the catalogue numbers MPLP: PS1 (541–11426), PS2 (544–11576), PS3 (546–11577), PS4 (552–11427), PS5 (555–11578), PS6 (557–11,579), PS7 (560–11,580), PS8 (562–11428), PS9(563–11429), PS10 (569–11581), PS13 (573–11582), PS14 (575,5–11431), PS15 (135–11588), PS16 (579, 5–11432), PS17(580–11433), PS18(580,5–11434), PS19 (583–11583), PS20 (585–11435), PS21(585,5–11436), PS22 (587,5–11584), PS23 (137–11589), PS24 (592–11585), PS25 (594,5–11586), PS26 (595, 5–11437), PS27 (139–11590), PS28(600,5–11438). Transmitted light microscopy was used to examine the organic particles on permanent strew slides. The relative percentage of OM components is based on counting at least 500 particles per slide using transmitted light microscopy. Palynofacies were categorized following Tyson (1995) and Batten (1996) into structured (palynomorphs, translucent and opaque phytoclasts) and structureless OM, commonly referred to as amorphous organic matter (AOM).

4. Results

On the basis of lithology, mineralogy and geochemistry the BORI was subdivided into two intervals: the Lower Interval (LI, 254.2–279.8 m from the base of the VMFm) and the Upper Interval (UI, 279.8–304.2 m).

4.1. Lithology and petrography

The studied section is constituted by a rhythmic alternation of mudstones, marls, calcareous marls and limestones (Fig. 2A and B), with interbedded calcite concretions, ash beds, calcite beef veins, and microbial bindstones. Ammonite fragments are common throughout the entire section. Ash beds are thin and continuous layers, argilized (Fig. 2C) or carbonatized during diagenesis. The argilized beds are white/yellow in color, thinner, softer, and more abundant throughout the section than the grey, hard, carbonatized beds. Occasionally, carbonatized ash beds may present load casts at their base. Calcite beef-veins are very common through the entire BORI. They average 3 cm in thickness and frequently show a bituminous layer in the middle of the vein (Fig. 2D).

The lowermost 2 m of the LI are characterized by microbial bindstones with an average thickness of 8 cm (Fig. 2E). Bindstones are constituted by millimetric laminae of organic-rich micrite intercalated with fine-grained micrite, with variable contribution of radiolarians, foraminifers, calcispheres and intraclasts (Kietzmann et al., 2018a, Fig. 4A and B). In occasions, bindstones present vertical fractures filled with calcite. In the lowermost 10 m of the LI, argilized ash beds and calcite concretions are very common. Above, the rest of the LI is mostly constituted of well-laminated, black to dark-grey marls and calcareous marls (average thickness 32 cm) which contain silt-sized detrital particles, mostly composed by quartz and feldspar, within an argillaceous-organic-rich matrix (Fig. 4C). Dark-grey, tabular, massive limestones (average bed-thickness 15 cm) are present throughout the entire LI, although they are less abundant than marls. The limestones are mostly radiolaritic wackestones (Fig. 4D and E) and, to a lesser extent, peloidal/intraclastic packstones/grainstones (Kietzmann et al., 2018a,

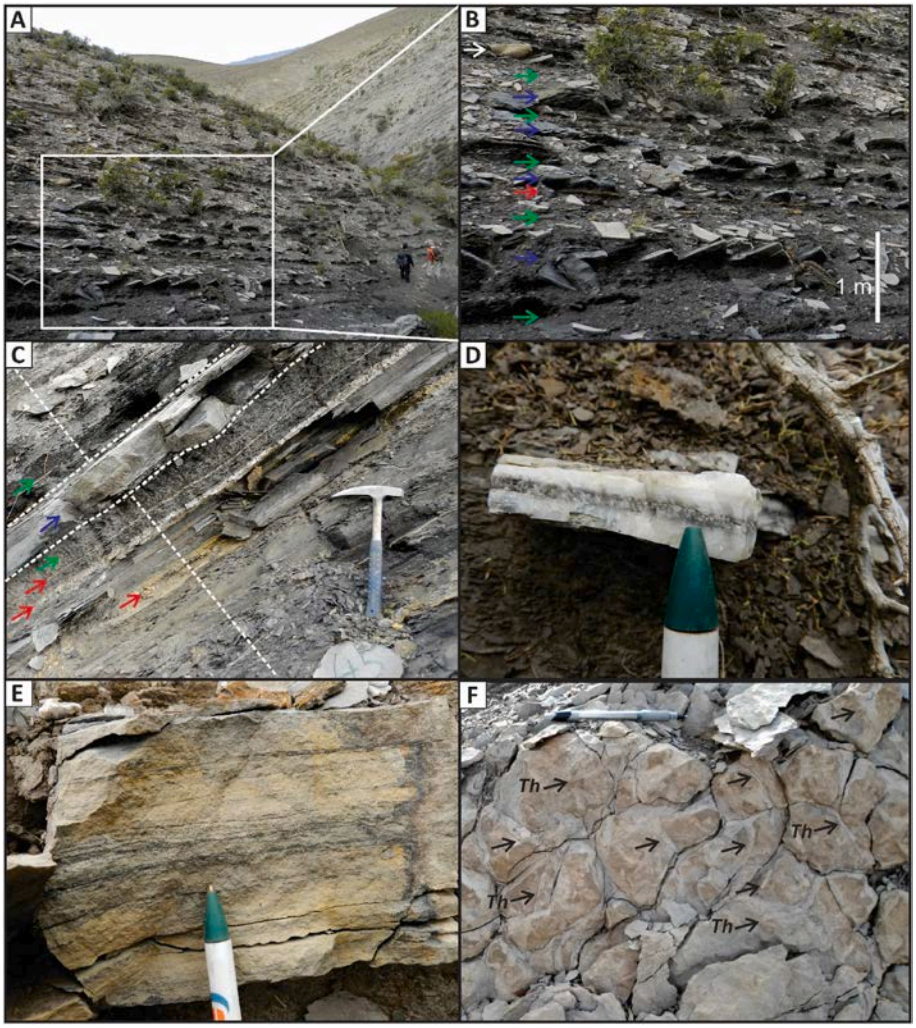

Fig. 2. Lithology of the BORI of the Vaca Muerta Fm in the Puerta Curaco section. **A**) General view of the studied section showing the rhythmic alternation of black, well-laminated marls and grey, well-laminated limestones. A close up view is shown in B. **B**) Detail of A showing the rhythmic succession of black marls (green arrows) with grey limestones (purple arrows), with occasional thin, reddish argilized ash beds (red arrow) and rounded calcite concretions (white arrow). **C**) Typical lithological arrangement for the BORI showing black, well-laminated marls (green arrows) and limestones (purple arrow) with interbedded thin whitish/reddish argilized ash beds. **D**) Fibrous calcite beef-vein characterized by a bituminous layer in the middle. **E**) Microbial bindstone constituted by the alternation of massive pure micrite with millimetric laminae of pure micrite and micrite with organic matter. **F**) Fully-bioturbated (*Thalassinoides*) limestones and calcite concretions preserved at the top of the BORI. *Th* = *Thalassinoides*.

Fig. 4F and G). Radiolarians (Spumellaria > Nasellaria) reach up to 80% of the total volume in the radiolaritic wakestones, and their tests are replaced by Fe-rich calcite and by green, sheet-like chlorite crystals (Fig. 4B and E).

The lowermost 3 m of the UI are dark marls and thin ash beds with rare diffuse ripple lamination (Fig. 3). Above, the rest of the UI mostly consists of dark, laminated calcareous marls, marls and limestones, similar to those described in the LI, although richer in calcite. Marls and limestones from this interval are mostly intraclastic/peloidal packstones/grainstones and, to a lesser extent, radiolaritic wackstones. The packstones/grainstones are constituted by highly deformed micritic peloids/intraclasts, with variable amount of radiolarians, bivalves, foraminifers and spicules, within an organic and detritus-rich matrix (Kietzmann et al., 2018a). The top of the UI is characterized by a 7 m-thick succession of calcareous marls and limestones, occasionally showing dense bioturbation (e.g., *Thalassinoides*; Fig. 2F). Marls are mostly constituted by fine-grained micrite, with variable contribution of detrital silt-sized particles of quartz and feldspar. Intraclasts oriented with it longest axis parallel to lamination and piritized calcispheres are minor components, whereas patches of microbioturbation in the form of small tubes are occasionally found (Fig. 4H).

4.2. Microfossil associations

Microfossil associations are moderately preserved, showing low abundance and diversity. Calpionellids comprise the upper *Calpionella* Zone (*Elliptica* Subzone) and the *Calpionellopsis* Zone, with *Simplex* and *Oblonga* Subzones, indicating a late Early to Late Berriasian age (Figs. 3 and 5). The *Elliptica* Subzone is characterized by *Tintinnopsella carpathica* (Murgeanu and Filipescu), *Calpionella alpina* Lorenz, and *Calpionella elliptica* Cadisch. The *Calpionellopsis* Zone include *Tintinnopsella carpathica*, *Calpionella elliptica*, *Tintinnopsella subacuta* (Colom), *Calpionella minuta Houša*, *Calpionellopsis simplex* (Colom) and *Calpionellopsis oblonga* (Cadisch).

Calcareous dinoflagellate cysts are distributed in two zones: The *Stomiosphaera wanneri* Zone (Early to early Late Berriasian), and *Colomisphaera vogleri-Colomisphaera conferta* Zone (Late Berriasian). The *Stomiosphaera wanneri* Zone contains *Stomiosphaera wanneri* Borza,

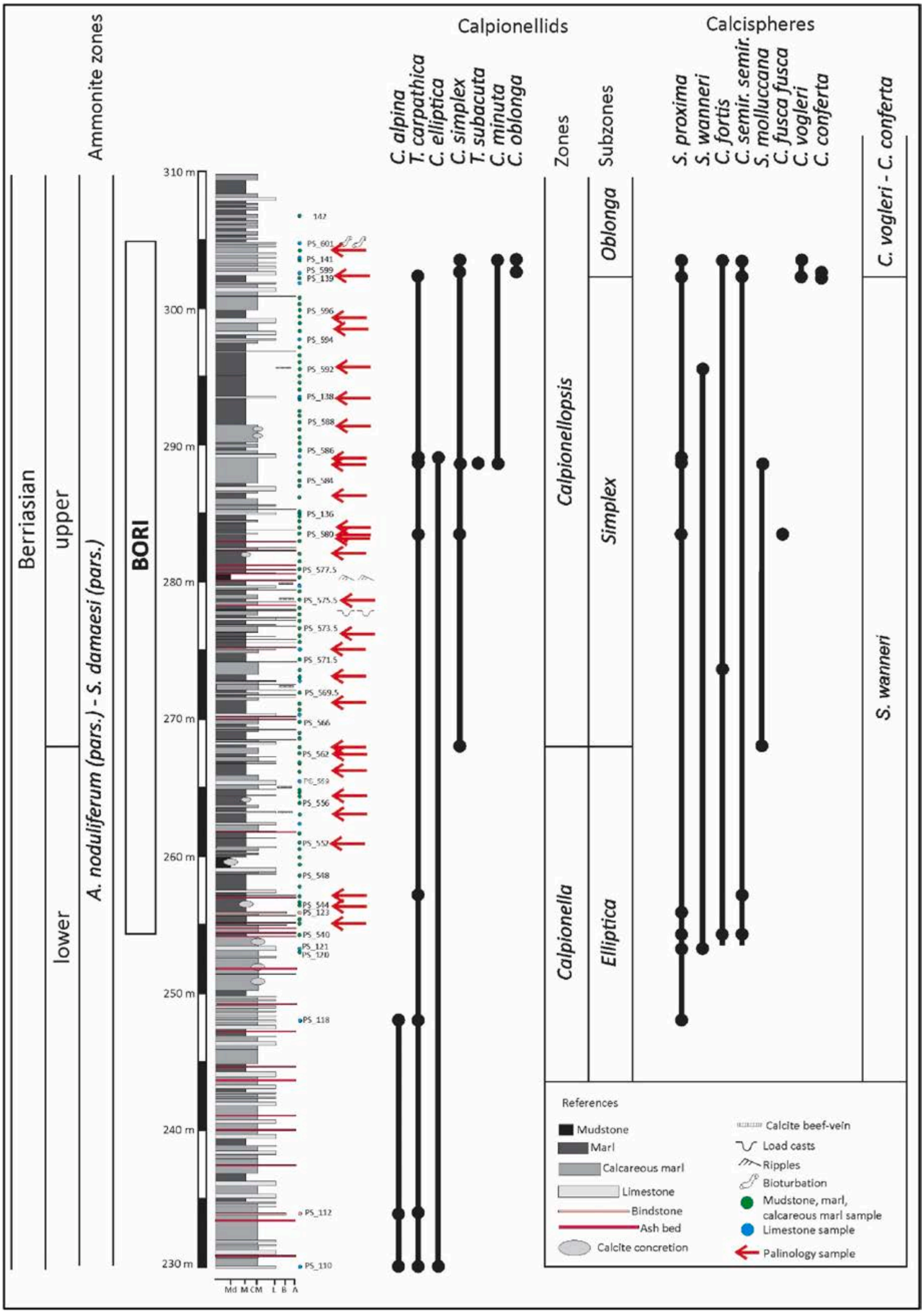

Fig. 3. Litholog of the BORl of the Vaca Muerta Formation in the Puerta Curaco section showing the distribution of species and zones of calpionellids and calcareous dinoflagellates. References: Md = mudstone, M = marl, CM = calcareous marl, L = limestone, B = bindstone, A = ash bed.

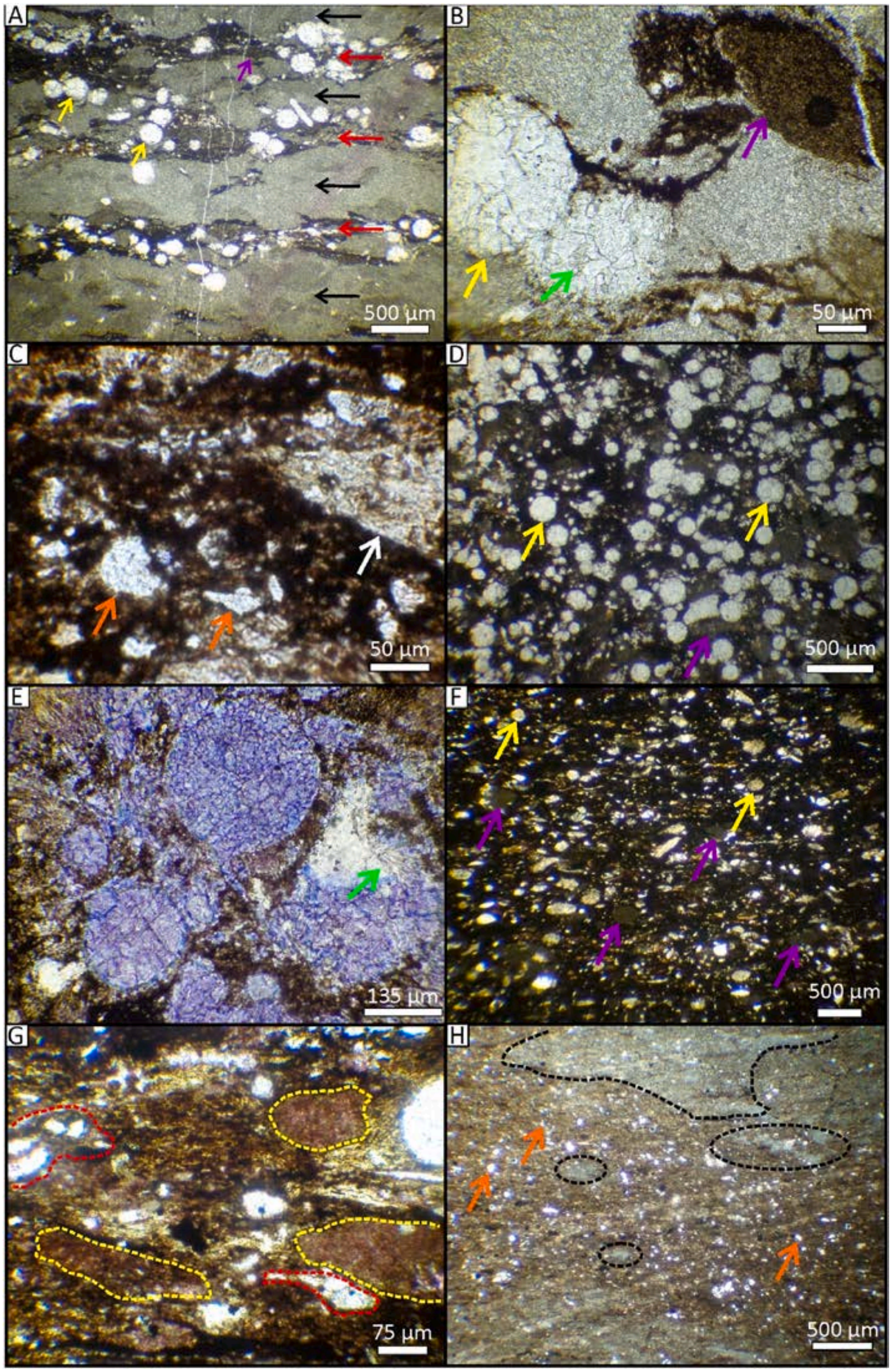

Fig. 4. Main microfacies of the BORI of the Vaca Muerta Formation in the Puerta Curaco section (uncrossed nicols). **A**) Microbial bindstone characterized by the alternation of millimetric bands of nearly pure micrite (black arrows) and organic-rich micrite (red arrows), carbonate peloids (purple arrow) and radiolarian tests (yellow arrows) (PS 123). **B**) Detail of A showing the alternation of pure micrite laminae with organic-rich micrite (purple arrow) and carbonate-replaced radiolarian (yellow arrow) occasionally exhibiting green, sheet-like chlorite crystals (green arrow) intergrown within calcite (PS 123). **C**) Mudstone characterized by silt-sized detrital particles of feldspar and quartz (orange arrows) and sand-sized intraclasts (white arrows) within an organic-rich matrix (PS 558). **D**) Radiolaritic wackestone composed of carbonate-replaced Spumellaria (yellow arrows) and to a lesser extent by rounded and deformed carbonatic peloids (purple arrows) and intraclasts (PS 127)**. E**) Detail of D showing the complete replacement of silica by Fe-rich calcite and sheet-like chlorite crystals (green arrow) in radiolaria (PS 127). **F**) Intraclastic/ peloidal packstone mainly composed by moderately compacted carbonatic intraclasts (purple arrows) with a relatively low contribution of radiolarians (yellow arrows) and silt-sized quartz and feldspar, within an organic-rich micritic matrix (PS 563). **G**) Detail of F showing the moderately compacted sand-sized carbonate peloids (yellow dashed outlines) with its longest axis oriented parallel to lamination, with variable contribution of sand intraclasts (red dashed outlines) and other detrital particles within an organic-rich, micritic matrix (PS 563). **H**) Bioturbated mudstone mainly composed of silt-sized quartz and feldspar (orange arrows) within a micritic matrix. Microbioturbation is present in the form of tubes and patches disrupting the original lamination of the rock (PS 141).

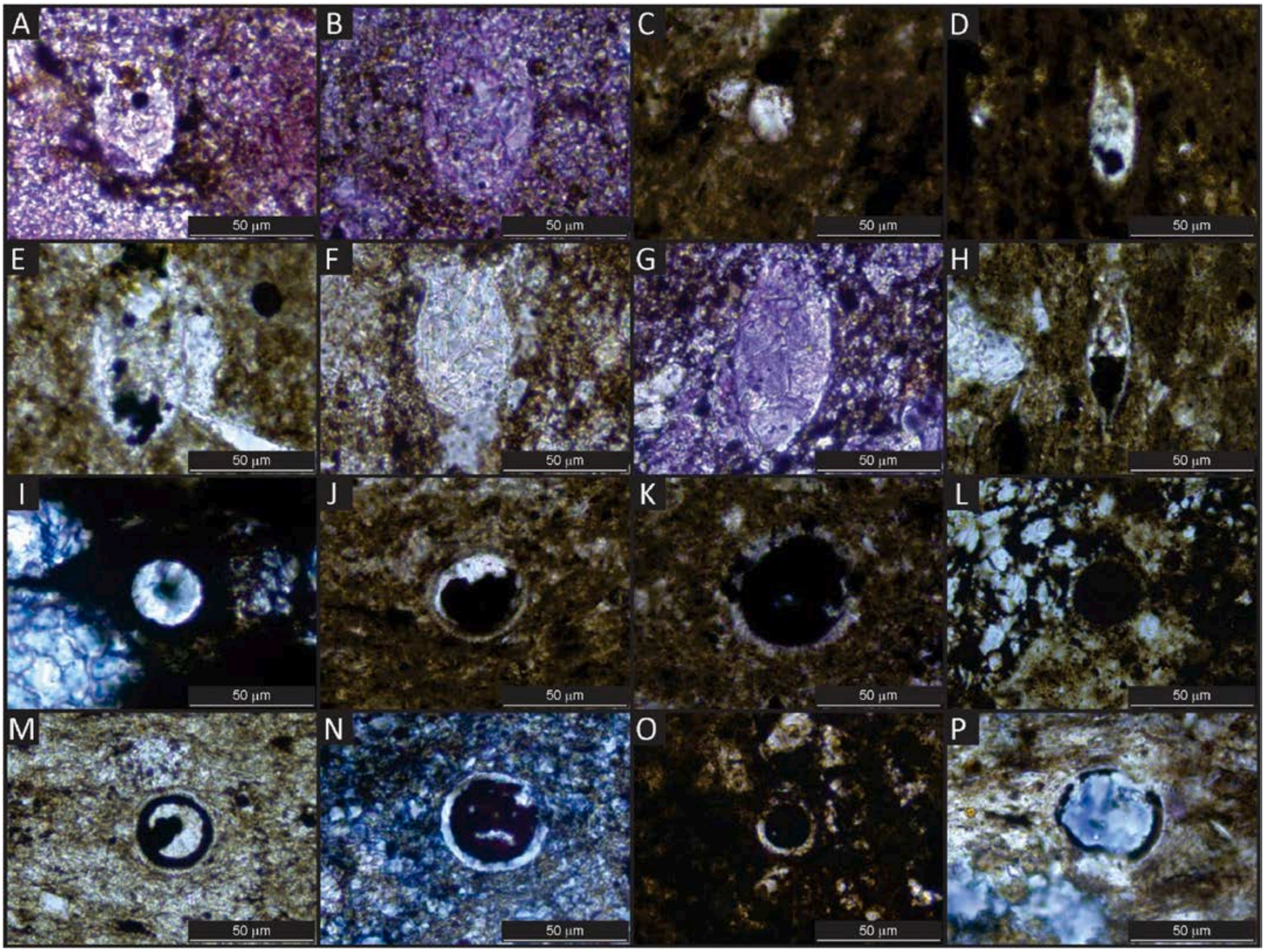

Fig. 5. Calpionellids and calcareous dinoflagellate cysts from the BORI of the VMFm in the Puerta Curaco section (uncrossed nicols). **A**) *Calpionella alpina* Lorenz, sample 112, *Elliptica* Subzone. **B**) *Calpionella elliptica* Cadisch, sample 110, *Elliptica* Subzone. **C**) *Calpionella minuta* Houša, sample 141, *Oblonga* Subzone. **D**) *Calpionellopsis oblonga* (Cadisch), sample 585, *Oblonga* Subzone. **E**) *Calpionellopsis simplex* (Colom), sample 599, *Oblonga* Subzone. **F**) *Tintinnopsella carpathica* (Murgeanu and Filipescu), sample 118, *Elliptica* Subzone. **G**) *Tintinnopsella longa* (Colom), sample 112, *Elliptica* Subzone. **H**) *Tintinnopsella subacuta* (Colom), sample 585, *Simplex* Subzone. **I**) *Cadosina fusca* Wanner, sample 580, *Wanneri* Zone. **J**) *Colomisphaera conferta* Řehánek, sample 599, *Vogleri-Conferta* Zone. **K**) *Colomisphaera fortis* Řehánek, sample 599, *Vogleri-Conferta* Zone. **L**) *Colomisphaera vogleri* (Borza), sample 599, *Vogleri-Conferta* Zone. **M**) *Crustocadosina semiradiata* (Wanner), sample 141, *Vogleri-Conferta* Zone. **N**) *Stomiosphaera moluccana* Wanner, sample 585.5, *Wanneri* Zone. **O**) *Stomiosphaera wanneri* Borza, samle 120, *Wanneri* Zone. **P**) *Stomiosphaerina proxima* Řehánek, sample 585, *Wanneri* Zone.

Stomiosphaerina proxima Řehánek, *Colomisphaera fortis* Řehánek, *Crustocadosina semiradiata* (Wanner), *Stomiosphaera moluccana* Wanner, and *Cadosina fusca* Wanner (Figs. 3 and 5). The *Colomisphaera vogleri* and *Colomisphaera conferta* are two separate zones, which could not be differentiated in this paper. This interval contains *Stomiosphaera wanneri* Borza, *Stomiosphaerina proxima* Řehánek, *Colomisphaera fortis* Řehánek, *Crustocadosina semiradiata* (Wanner), *Colomisphaera vogleri* (Borza) and *Colomisphaera conferta* Řehánek.

4.3. Spectral gamma-ray

The Total Gamma-Ray (TGR) values vary between 51 and 128 nSv/h (95 ± 19 nSv/h; Table 1 in Supplementary Material) throughout the entire BORI. TGR values are high and stable throughout the LI, commonly oscillating between 100 and 120 nSv/h (Fig. 6). In the UI, TGR values are lower and oscillate between 60 and 100 nSv/h (Fig. 6). The K content varies between 0.7 and 2.3 wt% (1.3 ± 0.3 wt%). In the LI, the K values are relatively stable and close to 1 wt%, whereas in the UI are higher, generally between 1 and 2 wt%. Th values oscillate between 4.8 and 13.9 (8.1 ± 1.9 ppm) and no meaningful change is observed between the LI and UI. Four ~ 5–10 m thick cycles (C1–C4) with increasing K and Th values are identified (Fig. 6). U values oscillate between 4.8 and 16.5 (10.2 ± 3.1 ppm) and they follow the same trend of the TGR values. U values are usually above 10 ppm in the LI and below 10 ppm in the UI (Fig. 6).

The Th/U ratio varies between 0.4 and 1.7 (0.9 ± 0.3) and is characterized by relatively low values in the LI (Th/U ~0.5) and higher values in the UI (Th/U ~1–1.5), clearly associated to the decrease of the U content towards the top of the BORI. The Th/U ratio also displays the same C1–C4 cycles described for the Th (Fig. 6). The (Th/K)*1000 ratio varies between 0.4 and 1.1 (0.6 ± 0.1) and shows relatively high values in the LI changing to lower and stable values in the UI. The C1, C2 and C3 cycles are also evident (Fig. 6).

4.4. Bulk and clay mineralogy

The bulk mineralogy of the mudstones, marls and calcareous marls is constituted of quartz (9–57 wt%), calcite (2–65 wt%), plagioclase (4–25

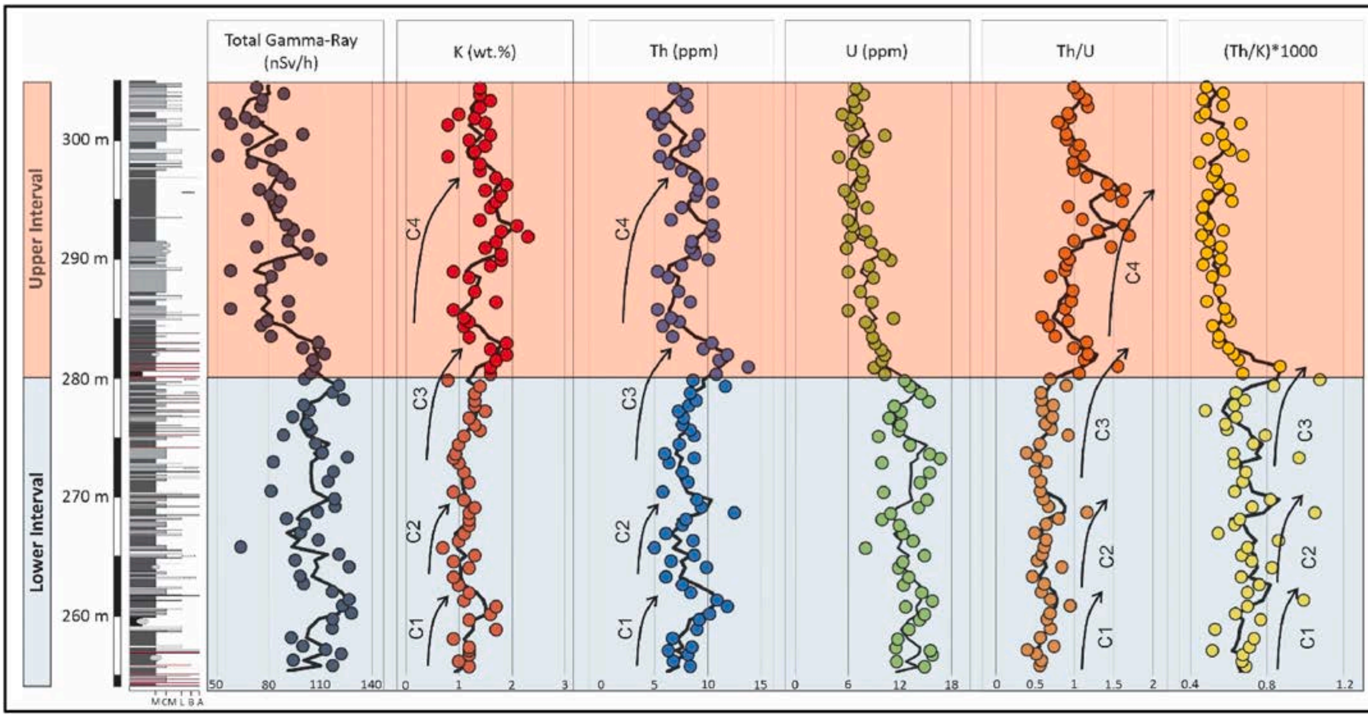

Fig. 6. Total and spectral gamma-ray values, Th/U and Th/K*1000 ratios of the BORI of the Vaca Muerta Formation in the Puerta Curaco section. The solid black line of each curve represents the moving average (3) and C1–C4 high-frequency cycles.

wt%), clay minerals (8–48 wt%), gypsum (0–11 wt%), fluorapatite (0–2 wt%) and pyrite (0–2 wt%). Additionally, dolomite is present in six samples, and its content oscillates between 1 and 4 wt% (Table 2 in Supplementary Material).

The highest values (30–50 wt%) of quartz are recorded in the LI and in the basal 3 m of the UI. Above, throughout the rest of the UI, quartz content is low, stable, and close to 10 wt% (Fig. 7). Calcite displays the opposite trend and is negatively correlated with quartz ($R^2 = 0.61$, $n = 52$). In the LI and in the basal 3 m of the UI, calcite values are relatively low (20–40 wt%), whereas in the rest of the UI vary between 40 and 60 wt%. Plagioclase content is highly variable throughout the entire BORI, but no substantial changes are identified between both intervals. The lowermost 3 m of the UI are characterized by high plagioclase content (up to 25 wt%; Fig. 7). The bulk clay mineral content is relatively stable and close to 20 wt% in the LI. Similarly to plagioclase, a 3 m-thick clay-rich interval is developed at the base of the UI. Above, throughout the rest of the UI, the average bulk clay mineral content oscillates between 25 and 35 wt% (Fig. 7). Neither quartz/plagioclase ($R^2 = 0.08$, $n = 52$) nor quartz/bulk clay mineral ($R^2 = 0.02$, $n = 52$) correlations are found, whereas a moderate positive plagioclase/clay mineral ($R^2 = 0.38$, $n = 52$) correlation is noticed. Gypsum is commonly present in the LI, whereas throughout the rest of the BORI its content is almost negligible. Pyrite is close to 1 wt% in the lowermost 15 m of the LI, whereas throughout the rest of the BORI its content is negligible. Fluorapatite is relatively high (0–2 wt%) in the lowermost 20 m of the LI and lower (0–1 wt%) throughout the rest of the BORI (Fig. 7).

The brittleness index varies between 0.21 and 0.64 (0.44 ± 0.10) in the LI and between 0.10 and 0.52 (0.21 ± 0.11) in the UI.

The clay mineralogy of both <2 μm and 2–16 μm size fractions consist of mixed-layer illite/smectite (I/S), illite, chlorite and kaolinite (Fig. 7, Table 3 in Supplementary Material). In both fractions the I/S presents an ordering type R3, where the abundance of illite layers within the I/S is higher than 90 % (Moore and Reynolds, 1997). No expandable layers are present in chlorite.

In the <2 μm fraction, I/S is the main clay mineral in all the samples. Its relative abundance varies between 30 and 100% (59% on average), with the highest value recorded in the lowermost sample (254.7 m), and relatively stable values close to 60% throughout the rest of the section. Chlorite is present in almost all the samples, varying between 0 and 70% (20% on average), and with no clear trend throughout the interval (Fig. 7). Illite is only absent in the lowermost 2 m of the BORI, its content varies between 0 and 51% (21% on average) and no clear trend is observed throughout the interval. Kaolinite is only identified in one sample (PS 552, 261 m) with a relative abundance of 28%.

In the 2–16 μm fraction I/S and chlorite are the main clay minerals in all the samples (Fig. 7). I/S is between 11 and 63% (34% on average) and chlorite is between 8 and 83% (39% on average). The LI is characterized by relatively high I/S and low chlorite contents, whereas the opposite is observed in the UI (Fig. 7). Illite is present in low concentrations (3–33%, 14% on average) in almost all the samples. Kaolinite (0–55%, 13% on average) is present in the LI and in the lowermost 3 m of the UI, whereas it is absent throughout the rest of the UI (Fig. 7).

In both size fractions the relative intensity of 002 peak of chlorite is lower (~50%) in the LI, than in the UI (~75%) as shown in Fig. 7.

4.5. Elemental geochemistry

ME and TE (Fig. 8) were grouped based on their geochemical affinity into four groups: siliciclastic, carbonate, organic and sulfide (e.g., Algeo and Maynard, 2004; Tribovillard et al., 2006; Calvert and Pedersen, 2007).

Siliciclastic group: Al, K, Si, Na and Mg integrate this group and they are usually the major constituents of the clayey, silty and siliciclastic particles of the rock (Calvert and Pedersen, 2007). Al content varies between 1.48 and 9.05 wt% (4.49 ± 1.59 wt%; Table 4 in Supplementary Material), no clear trend is recorded throughout the BORI, and values are lower than the Al content of the AS (Fig. 8A). Si values vary between 8.51 and 28.52 wt% (18.45 ± 5.33 wt%). They show a low and positive correlation with Al ($R^2 = 0.19$, $n = 43$) and display a general decreasing trend from the base towards the top of the interval (Fig. 8A). The Si/Al ratio displays the same trend than Si absolute values, being higher than that of the AS in the LI, slightly higher in the basal 10 m of

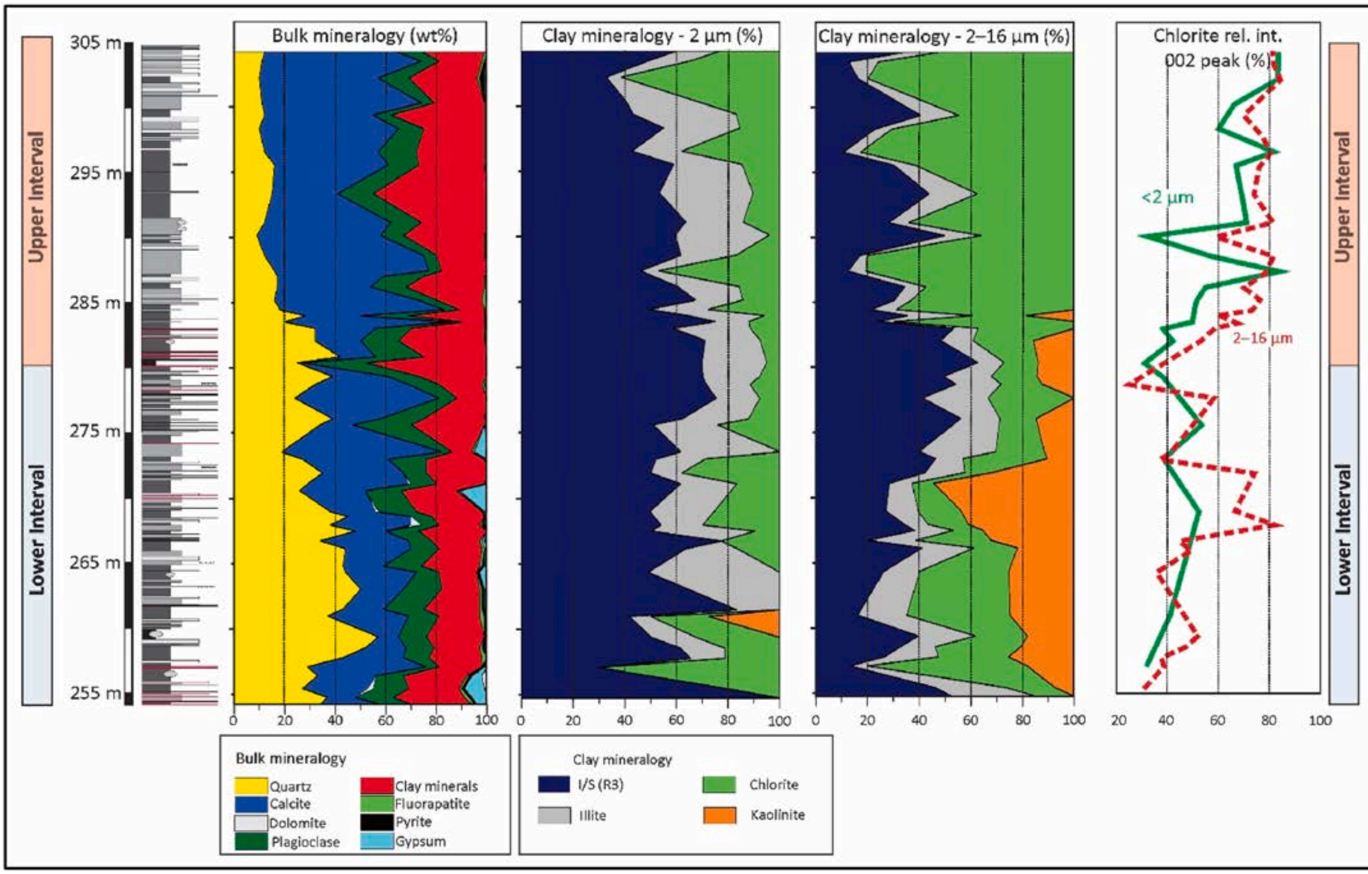

Fig. 7. Bulk and clay mineralogy of the BORI of the Vaca Muerta Formation in the Puerta Curaco section. References: rel. int. = relative intensity.

the UI (280–290 m) and lower in the rest of the UI (290–305 m). The calculated Si_{excess} values vary between 0 and 13.79 wt%. Si_{excess} display a decreasing trend towards the top of the BORI, indicating no Si enrichment in the upper part of the UI (290–305 m). K content varies between 0.27 and 2.15 wt% (1.05 ± 0.44 wt%) and exhibits a very good and positive correlation with Al ($R^2 = 0.95$, $n = 43$). Absolute values display a subtle increasing trend throughout the BORI, with values generally between 0.5 and 1.25 wt% in the LI, higher and close to 1.7 wt % in the lowermost 5 m of the UI (280–285 m), close to 0.7 wt% in the middle part of the UI (285–290 m) and close to 1.25 wt% in the upper part of the UI (290–305 m). The K/Al ratio displays an increasing trend throughout the interval although values are always lower than those of the AS (Fig. 8A). Na values vary between 0.28 and 1.50 wt% (0.75 ± 0.27 wt%) and show good positive correlation with Al ($R^2 = 0.68$, $n = 43$). Absolute values do not show any vertical trend throughout the BORI, whereas the Na/Al ratio exhibits a general decreasing trend from the base to the top (Fig. 8A). In the LI and in the basal 10 m of the UI, the Na/Al ratio is higher than that of the AS, whereas in the upper part of the UI the Na/Al ratio is very close to that of the AS. Mg content varies between 0.29 and 0.98 wt% (0.55 ± 0.16 wt%) and exhibits a moderate and positive correlation with Al ($R^2 = 0.38$, $n = 43$). This correlation is considerably higher ($R^2 = 0.63$, $n = 40$) when samples with dolomite are excluded from the analysis (samples: PS 563-569-580). Absolute values are relatively low and stable (~0.4–0.6 wt%) throughout the BORI although two intervals with higher values (>0.6 wt%) are identified in the UI: 280–285 m and 293–303 m (Fig. 8A). The Mg/Al ratio is relatively constant and lower than that of the AS except for two intervals with small amounts of dolomite, where the ratio is similar or slightly higher than that of the AS (Fig. 8A). Fe content varies between 0.91 and 4.05 wt% (2.16 ± 0.63 wt%) and displays a good and positive correlation with Al ($R^2 = 0.56$, $n = 43$). Fe absolute values are relatively low (~1–2 wt%) in the LI and in the basal 10 m of the UI, and relatively higher (~2–3 wt%) in the rest of the UI. The Fe/Al ratio is always higher than that of the AS and displays two subtle increasing cycles in the LI. Above, in the UI, the Fe/Al ratio is stable and close to 0.45 (Fig. 8A).

Carbonate group: Ca, Mn and Sr integrate this group, since these elements are major constituents of the carbonate fraction (e.g., calcite, dolomite) of the rocks. Ca values vary between 1.42 and 27.77 wt% (14.82 ± 6.67 wt%; Table 4 in Supplementary Material) and display a very good and negative correlation with Si ($R^2 = 0.92$, $n = 43$). Absolute values display three increasing cycles: one in the LI (255–277 m) and two in the UI (277–290 m and 290–305 m). The Ca/Al ratio displays two increasing/decreasing cycles: one in the LI (255–280 m) and the other in the lower part of the UI (280–290 m), whereas in the rest of the UI the Ca/Al ratio is relatively stable and close to 4 (Fig. 8B). The Ca/Al ratio is always higher than that of the AS. Sr content varies between 161.0 and 390.4 ppm (261.9 ± 50.4 ppm) and displays a rough and positive correlation with Ca ($R^2 = 0.40$, $n = 43$). Absolute values are relatively low (~225 ppm) in the lowermost 5 m of the LI and higher (~270 ppm) and stable throughout the rest of the section. The Sr/Al ratio is characterized by relatively high values in the lowermost 5 m of the LI (255–260 m). Above, it displays a general increasing trend throughout the rest of the LI, followed by a quick drop in the basal 5 m of the UI (280–285 m). Above, the Sr/Al ratio displays a general decreasing trend throughout the rest of the UI. The Sr/Al ratio is always higher than that of the AS. The Sr/Ca ratio is relatively low (~0.002) and stable throughout the whole section, except in the basal UI (279–284 m), where values are considerably higher (~0.009). Mn content varies between 0.01 and 0.08 wt% (0.04 ± 0.02 wt%) and shows a good and positive correlation with Ca ($R^2 = 0.50$, $n = 43$). Absolute values are relatively low (~0.01–0.02 wt%) in the LI and in the lower part of the UI, whereas they are considerably higher (~0.04–0.07 wt%) throughout the rest of the UI

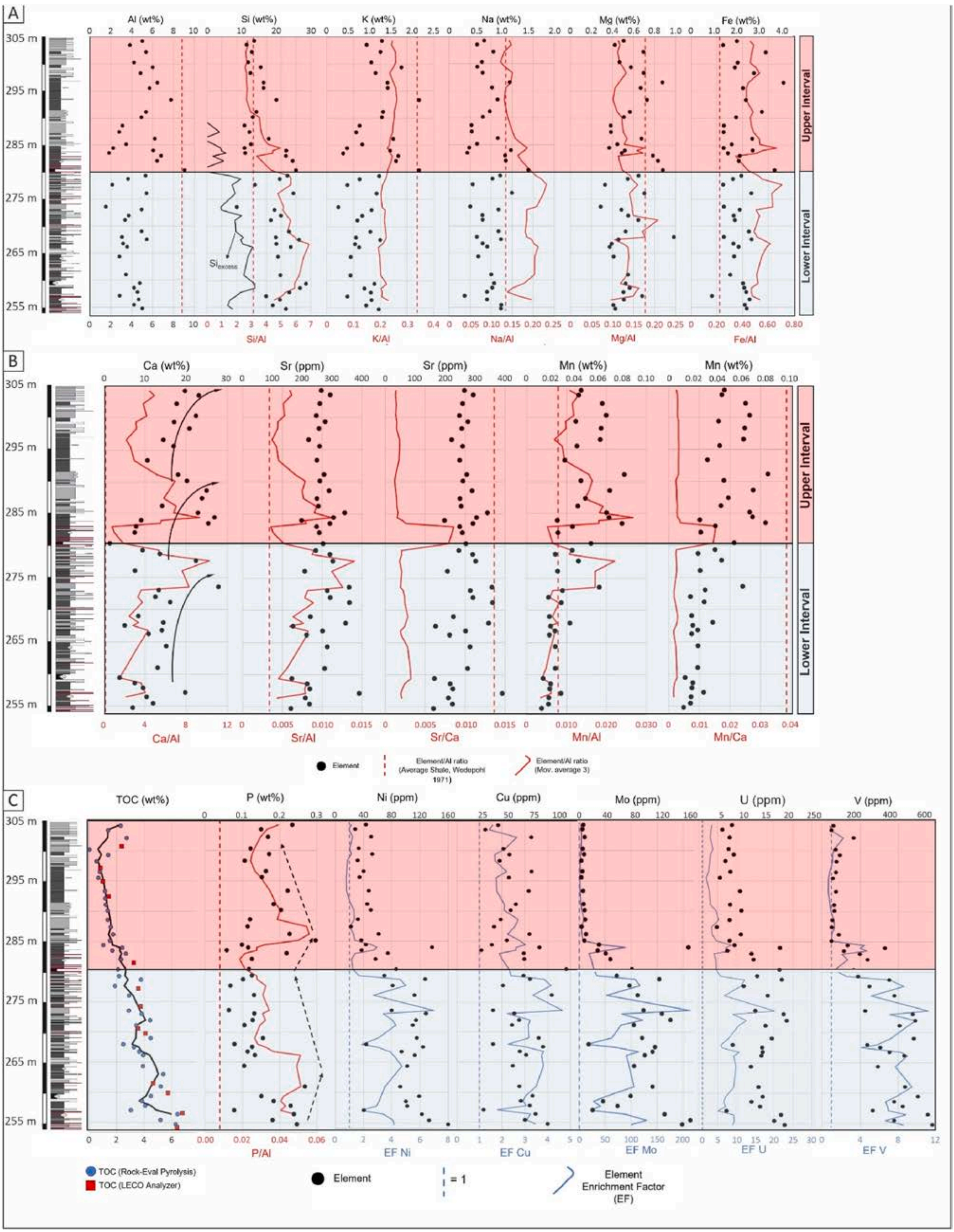

Fig. 8. ME and TE of the BORI of the Vaca Muerta Formation in the Puerta Curaco section. **A**) Al, Si, K, Na, Mg and Fe content, representative of the Siliciclastic group. **B**) Ca, Sr and Mn content, grouped in the Carbonate group. **C**) TOC, P, Ni, Cu, Mo, U and V content and their enrichment factors (EF). These elements are part of the Organic and Sulfide groups.

(Fig. 8B). The Mn/Al ratio displays the same trend than the Sr/Al ratio and values can be lower or higher than those of the AS (Fig. 8B). The Mn/Ca ratio displays the same trend than Sr/Ca with values always lower than those of the AS (Fig. 8B).

Organic and sulfide groups: Mo, U, V, Zn, Ni, Cu and P integrate this group (Table 5 in Supplementary Material). These elements are associated since they are frequently enriched in sediments with high amounts of OM, deposited under anoxic conditions, or both (e.g., Wignall and Myers, 1988; Algeo and Maynard, 2004; Tribovillard et al., 2006; Föllmi, 1996).

Mo content varies between 3.4 and 160.1 ppm (56.5 ± 49.9 ppm) and shows a positive correlation with the TOC content ($R^2 = 0.62$, $n = 43$). Absolute values display a general decreasing trend, with the highest values (Mo ~40–160 ppm) in the LI and in the lowermost 4 m of the UI, and lower values (Mo < 10 ppm) in the rest of the UI. The enrichment factor (EF) of Mo varies between 2 and 212 and follows the same vertical trend than that of absolute values (Fig. 8C). U content varies between 4.0 and 19.4 ppm (11.3 ± 4.6 ppm) and presents a good and positive correlation with TOC ($R^2 = 0.58$, $n = 43$). Absolute values are relatively high and stable (~10–20 ppm) in the LI and in the lowermost 5 m of the UI, with a sharp decrease (~5–10 ppm) in the rest of the UI. The EF U varies between 2 and 20 and displays a general increasing trend from 255 to 275 m and a decreasing trend between 275 and 285 m. Above and throughout the rest of the UI, the EF U is relatively low and stable, between 2 and 4. V absolute values vary between 52.7 and 624.4 ppm (267.2 ± 179.9 ppm) and present a very good and positive correlation with the TOC ($R^2 = 0.85$, $n = 43$). V absolute values display the same vertical trend than that of Mo, with high values (~200–600 ppm) in the LI and in the lowermost 5 m of the UI, and low values (~50–100 ppm) in the rest of the UI (Fig. 8C). The higher EF V values are recorded in the lower part of the LI (255–275 m), then they decrease in the lowermost 5 m of the UI and are close to 1 in the rest of the UI (Fig. 8C).

The absolute content of P varies between 0.06 and 0.30 wt% (0.15 ± 0.06 wt%; Table 4 in Supplementary Material). No correlation with the TOC content ($R^2 = 0.06$, $n = 43$) and a rough and positive correlation with Al ($R^2 = 0.43$, $n = 40$) are observed when three outliers are excluded of the analyses. P absolute values display two increasing/decreasing cycles: the first one is developed in the LI and in the lowermost 5 m of the UI and the second one in the rest of the UI (Fig. 8C). The P/Al ratio displays a similar trend than P absolute values and the P/Al ratio is always higher than that of the AS (Fig. 8C). Ni absolute values vary between 21.9 and 159.8 ppm (77.2 ± 38.0 ppm) and present a good positive correlation with the TOC content ($R^2 = 0.69$, $n = 43$). The highest values (Ni ~80–120 ppm) are recorded in the LI (Fig. 8C). Above, in the lowermost 5 m of the UI, values are lower and oscillate between 80 and 40 ppm. In the rest of the UI, absolute values are even lower and vary between 20 and 50 ppm. The EF Ni values vary between <1 and 11 and increase throughout the lower and middle part of the LI (255–274 m). Above, the EF Ni decreases towards 1 in the upper part of the LI and in the lower part of the UI (274–285 m). The EF Ni is stable, close to 1 or slightly lower throughout the rest of the UI (Fig. 8C). Cu values vary between 23.6 and 105 ppm (58.7 ± 18.56 ppm) with a rough positive correlation with TOC ($R^2 = 0.19$, $n = 43$), a good positive correlation with Al ($R^2 = 0.46$, $n = 43$) and no clear vertical trend (Fig. 8C). The EF Cu varies between 1 and 5 and with relatively high values in the LI and relatively low values in the UI (Fig. 8C). Zn absolute values oscillate between 5.7 and 667.5 ppm (110.4 ± 140 ppm) and present a low, positive correlation with TOC ($R^2 = 0.13$, $n = 43$). Absolute values are variable throughout the entire BORI, although the highest values (>200 ppm) are generally in the lower and middle part of LI (255–270 m). Above, in the rest of LI and in the UI, absolute values are generally lower than 100 ppm, although they may peak up to 347 ppm. The EF Zn varies between <1 and 16 and follows a similar trend than that described for the absolute values.

4.6. Rock-Eval pyrolysis and carbon and oxygen isotopic composition

The TOC content varies between 0.01 and 6.76 wt% (2.94 ± 1.69 wt %) whereas the calculated original TOC content (TOC_o) varies between 3 and 14 wt% (8 ± 3 wt%; Table 6 in Supplementary Material). The TOC content displays a clear decreasing trend from 255 to 300 m, followed by a subtle increase between 300 and 305 m (Fig. 9). T_{max} values are generally higher than 470 °C (514 ± 17 °C), whereas HI varies between 7 and 31 mg HC/g TOC and OI between 16 and 125 mg CO_2/g TOC (Table 6 in Supplementary Material). The low HI values precluded determination of the kerogen types (Capelli et al., 2021).

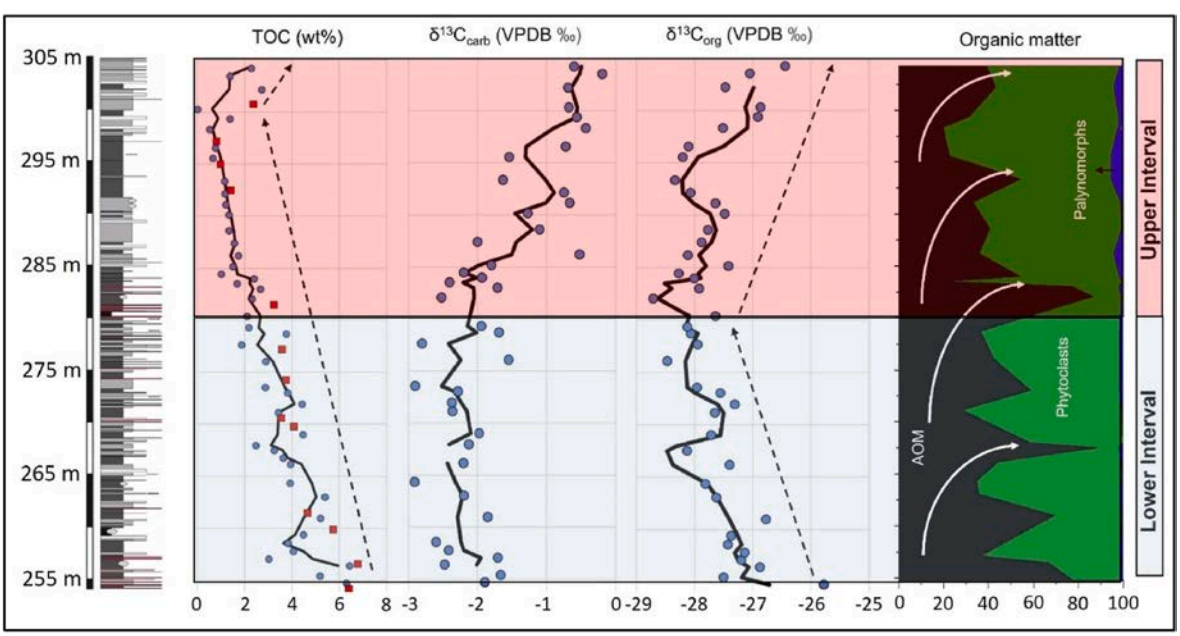

Fig. 9. TOC, $\delta^{13}C_{carb}$, $\delta^{13}C_{org}$ and palynological analyses of the BORI of the Vaca Muerta Formation at Puerta Curaco section. In the $\delta^{13}C_{org}$ curve, two samples (PS563 at 268 m and PS580 at 283.5 m), with low $\delta^{13}C_{org}$ values (−29.6 and −29.3‰ respectively), are out of scale. The solid and black line in each track is the 3-point moving average and the red squares in the TOC track show the TOC determined by LECO analyzer. AOM = amorphous organic matter.

The $\delta^{13}C_{carb}$ values range from −2.9 to −0.2‰ (−1.7 ± 0.8‰) in the BORI. In the LI and the lowermost 5 m of the UI $\delta^{13}C_{carb}$ values oscillate between −2 and −3‰, whereas in the rest of the UI they are higher and display a general increasing trend towards the top (from ~ −2 to −0.5‰). The $\delta^{18}O_{carb}$ values range between −9.9 and −7.4‰ (−8.4 ± 0.5‰) and are not significantly correlated with the $\delta^{13}C_{carb}$ values ($R^2 = 0.12$, $n = 41$). In the LI, $\delta^{18}O_{carb}$ values are relatively low and vary between −9 and −8.5‰, whereas in the UI values are relatively higher and between −8.5 and −7.5‰. The $\delta^{13}C_{org}$ values range from −29.6 to −25.8‰ (−27.7 ± 0.7‰). The base of the LI is characterized by relatively high values (~−27‰) followed by a general decreasing trend towards the top of the interval, where values are close to −28‰ (Fig. 9). The $\delta^{13}C_{org}$ values of the UI develop a general increasing trend, with lower values at the base (−28‰) and higher values towards the top (~−27‰; Fig. 9; Table 6 in Supplementary Material).

4.7. Palynology

Visual observations suggest that three groups of dispersed OM are important in nearly all the samples: phytoclasts, AOM and palynomorphs (Fig. 9; Table 7 in Supplementary Material). Phytoclasts are the most abundant type of OM in the BORI. They are present as small (5–20 μm in diameter), equidimensional, mostly opaque, fragments with angular, and sometimes corroded edges (Fig. 10B and C). Translucent phytoclasts are less abundant and they only represent the 0.1–3% of the total phytoclasts content, whereas large blade-shaped individuals are rare. The content of phytoclasts varies between 9.8 and 81% (51 ± 19.2%) and the highest values are generally recorded in the UI, especially from 285 m onwards (Fig. 9), where phytoclasts can reach up to 100 μm in diameter. The AOM is the second most abundant type of OM throughout the interval. It is mainly of granular type, finely divided and appears in aggregate masses (Fig. 10A and C). Its content fluctuates between 18.8 and 88.4% (47.4 ± 19.4%), and the highest values are recorded in the LI and in the lowermost 5 m of the UI (Fig. 9). Palynomorphs (Fig. 10D–H) are represented by continental pollen grains (*Classopollis, Callialasporites*) and by marine components (small acritarchs of 10–12 μm in diameter, dinocysts, tasmanitids, and prasinophycean algae). Among dinocysts, specimens of the Berriasian taxon *Cribroperidinium reticulatum* were recognized (Fig. 10D). The relative abundance of the palynomorphs within the BORI is low and varies between 0 and 5.4% (1.6 ± 1.4%) and they are essentially present in the UI (Fig. 9), mainly constituted by small acritarchs (Fig. 10G and H).

5. Discussion

5.1. Diagenetic overprint in the mineralogy and geochemistry of the BORI

The primary mineralogy and geochemistry of the BORI of the VMFm in Puerta Curaco section has been affected by early and late diagenetic processes. The latter took place in deep-burial conditions, with estimated temperatures between 150 and 200 °C (Catalano et al., 2018; Weger et al., 2019; Capelli et al., 2021), in agreement with the regional maturity trend calculated for the VMFm (Brisson et al., 2020; Spacapan et al., 2021). The high diagenetic grade reached by the VMFm in the Puerta Curaco section is evidenced in the T_{max} values (>470 °C) measured from Rock-Eval pyrolysis, which indicate that OM is overmature (dry gas window stage), thus inhibiting determination of the kerogen type (e.g., Espitalié et al., 1985; Tissot and Welte, 1984; Peters and Cassa, 1994). Additionally, this resulted in relatively low values of TOC (3 wt% on average), compared to the calculated TOC_o (8 wt% on average), because a considerable part of the original OM was transformed to hydrocarbons or released to the system as CO_2 during burial.

The main diagenetic processes affecting the primary mineralogy of the BORI of VMFm are: 1) precipitation of carbonates, 2) precipitation of quartz, 3) transformation of K-feldspars and zeolites to albite, and 4) transformation of clay minerals (Capelli et al., 2018, 2021; Catalano et al., 2018; Rodriguez Blanco et al., 2018). Calcite is the main mineral in the marls and mudstones of the BORI (34 wt% on average) and is present in multiple forms including fine-grained micrite, peloids, primary bioclasts, or as fillings and replacements in radiolarians (Fig. 4A–E and G). The general increasing trend of the $\delta^{13}C_{carb}$ values observed throughout the BORI, opposite to the decreasing trend of the TOC content (Fig. 9), suggests that an important amount of calcite, especially in the LI, was formed during diagenesis through the oxidation of organic C (e.g., Scasso et al., 2002; Catalano et al., 2018; Rodriguez Blanco et al., 2018, 2022a; Ravier et al., 2020; Lanz et al., 2021). A broad, negative

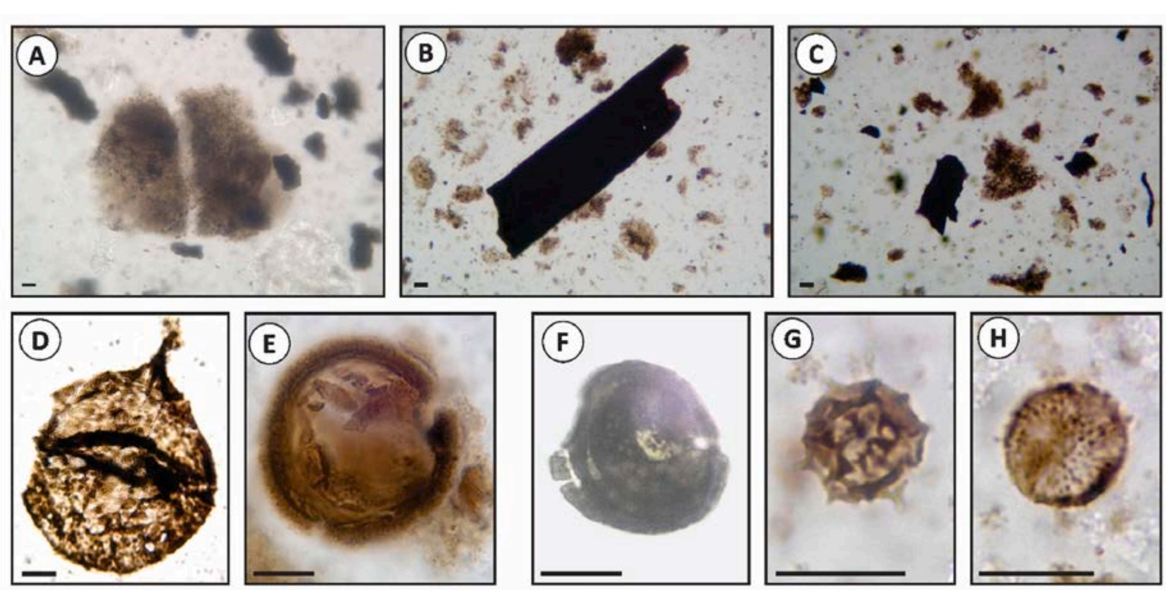

Fig. 10. Palynomorphs and palynofacies assemblages from the BORI of the Vaca Muerta Formation in Puerta Curaco section. **A)** Granular AOM in the center and equidimensional opaque phytoclasts PS2: M34/0. **B)** Very large blade-shaped opaque phytoclast (200 μm) PS28: G41/2. **C)** General view of granular AOM and equidimensional and blade-shaped phytoclasts PS10: D40/3. **D)** *Cribroperidinium reticulatum* Quattrocchio and Volkheimer, PS23: B46/3(dinocyst). **E)** *Tasmanites* sp. PS26: K40/0 (prasinophycean algae). **F)** *Classopollis* sp. PS23: J39/0 (pollen grain). **G-H)** Small acritarchs. **G)** *Micrhystridium* sp. PS26: T32/0. **H)** *Mecsekia* sp. PS26: PSW31/4. Scale bar = 10 μm.

correlation between $\delta^{13}C_{carb}$ and TOC content was observed throughout the entire BORI ($R^2 = 0.3$, $n = 41$), where higher TOC values are associated with relatively low $\delta^{13}C_{carb}$ values. Conversely, compared to the LI, the higher $\delta^{13}C_{carb}$ values of the UI must be related to a greater contribution of primary carbonate (Scasso et al., 2002; Rodriguez Blanco et al., 2018). Ca for calcite precipitation was mostly provided by dissolution of calcareous skeletons and, to a lesser extent, by the albitization of plagioclase. Low amounts (1–4 wt%) of dolomite were found in only six samples of marls and mudstones of the BORI (Fig. 7). This is queer because in less-diagenized sections of the VMFm (oil window zone) dolomite content may reach up to 40 wt% (González et al., 2016; Rosemblat et al., 2016). The very low content of dolomite in the overmature rocks of the BORI may indicate dedolomitization between the oil and the dry gas zones. Those samples lacking dolomite present an average Mg/Al ratio of 0.13 (n = 48), whereas the sample with the highest dolomite content (4 wt%, PS 563; Fig. 8A) presents the highest Mg/Al ratio (0.32) from the entire BORI. This suggests that the Mg/Al ratio can be used as a proxy to track the presence of dolomite in marls and mudstones of the VMFm.

The lack of correlation between Si and Al ($R^2 = 0.19$, $n = 43$) indicates that a considerable part of Si in the marls and mudstones of the VMFm presents a non-detrital, biogenic origin (e.g., Ross and Bustin, 2009; Dong et al., 2018). The significative source of additional Si in these rocks are the radiolarian skeletons present in the radiolaria-rich facies, whose tests were replaced by calcite during the early diagenesis (Fig. 4E). The dissolved Si later precipitated as fine-grained, euhedral crystals of quartz in the matrix (Scasso et al., 2002; Catalano et al., 2018; Milliken et al., 2019; Capelli, 2021).

Transformation of K-feldspar and zeolites to albite (e.g., Land and Milliken, 1981; Boles, 1982; Utada, 2001) also occurred during deep burial of the marls and mudstones in Puerta Curaco section. The XRD analyses revealed only plagioclase feldspar, suggesting that detrital, original K-feldspar was transformed to albite, releasing K^+ to porewaters (e.g., Hower et al., 1976; Land and Milliken, 1981; Boles, 1982). In this reaction, the Na^+ needed for albitization is available from porewaters through the transformation of smectite to illite (e.g., Hower et al., 1976; Boles and Franks, 1979; Boles, 1982). In addition, a meaningful amount of albite may have been formed through the transformation of Na-rich zeolites, like analcime (e.g., Iijima, 1988; Utada, 2001). This is supported by the fact that analcime is frequently present in the marls and mudstones of the VMFm in sections submitted to a lower diagenetic grade than that of Puerta Curaco section (Capelli, 2021). The complete absence of zeolites in the overmature rocks of Puerta Curaco section suggests that transformation of Na-zeolites to albite occurred well before the rocks attained their maximum burial temperatures.

The clay mineralogy of the BORI in Puerta Curaco section is mostly constituted by high-ordered mixed-layer I/S and chlorite, a classic clay mineral association of deeply-buried successions (e.g., Dunoyer de Segonzac, 1970; de Barrio et al., 2018; Hower et al., 1976; Chamley, 1989). The high-ordering (R3 type) of the I/S in the marls and mudstones of the VMFm is a consequence of the illitization of smectite (Capelli et al., 2020). This is confirmed by the predominance of smectite in less-diagenized sections of the VMFm elsewhere (Scasso et al., 2002, 2005; Krim et al., 2017, 2019; Capelli, 2021). In addition, the excellent correlation between Al and K ($R^2 = 0.95$, $n = 43$) indicates that the main clay mineral in the BORI is I/S. The relative intensity of the 002 peak suggests that two types of chlorites are present: an Al–Mg-rich chlorite (sudoite) and a Fe-rich chlorite. Sudoite is observed in the radiolarian tests of the marls and mudstones (Fig. 4B and E) and was also documented in overmature marls and mudstones of the VMFm in the Chacay Melehue section, 48 kms to the west of Puerta Curaco, and in carbonatized ash beds of both, the Chacay Melehue and Puerta Curaco sections (Capelli et al., 2020, 2021; Kietzmann et al., 2021a). According to these authors, the origin of sudoite in the carbonatized ash beds is related to *in situ* precipitation from Al-, Mg-, and Si-rich porewaters during late diagenetic stages. The same process is proposed for the sudoite in marls and mudstones of the BORI. Here, sudoite is more abundant in marls of the LI, which contain kaolinite in the 2–16 μm size fraction, but not in the <2 μm size fraction (Fig. 7). This indicates that at least some of the sudoite present in the marls may have been formed throughout the transformation of former kaolinite during burial (e.g., Hillier et al., 2006; Beaufort et al., 2015). This transformation would have been totally accomplished in the more reactive, smaller, clay particles less than 2 μm in diameter, but not in the larger particles between 2 and 16 μm. Further studies are needed to confirm this. On the other hand, the Fe-rich chlorites, more abundant in the UI, were probably formed through the transformation of Fe-rich clay precursors in the original sediments, like odinite and berthierine (e.g., Ehrenberg, 1993; Baker et al., 2000). The increment of the absolute values of Fe reported in the UI (2.29 wt% on average) compared to those in the LI (2.04 wt% on average) is in agreement with the increment of Fe-rich chlorite reported in the UI of the BORI (Figs. 7 and 8A).

5.2. Paleoenvironment: oxygenation, productivity, and organic matter accumulation

The paleoenvironmental reconstructions for the whole VMFm in Puerta Curaco section indicate that sedimentation took place in a basinal to outer carbonate ramp environment characterized by overall sea bottom anoxia and high sea water productivity (DÓdorico, 2009; Kietzmann et al., 2016; Capelli et al., 2018; Catalano et al., 2018). Most of the sedimentation occurred from suspension of the water column and from occasional reworking of shallow-water sediments by storm-generated turbidity flows (Kietzmann et al., 2016).

The study of the redox sensitive trace elements (RSTE) in mudstones has been widely used to reconstruct the past ocean oxygenation and productivity of the water column (e.g., Wignall and Myers, 1988; Algeo and Maynard, 2004; Tribovillard et al., 2006; McArthur, 2019). The analyses of the RSTE to infer the paleoredox conditions of accumulation of the VMFm was also applied in other stratigraphic intervals elsewhere (e.g., Spalletti et al., 2014, 2019; Krim et al., 2017, 2019; Capelli et al., 2018, 2020; Musacchio et al., 2022) and may contribute to a better understanding of the depositional environment of the BORI. Mo, U, and V have low solubility under reducing conditions and sediments deposited in anoxic-sea bottom environments are frequently enriched in them (e.g., Tribovillard et al., 2006). On the other hand, Ni, Cu, and Zn are frequently sourced to the sediments in association with OM, and thus, they are usually used as paleoproductivity proxies (Algeo and Maynard, 2004; Tribovillard et al., 2006). Si_{excess} is also associated with high productivity of the sea water (e.g., Ross and Bustin, 2009; Dong et al., 2018). In addition to the study of the RSTE, the quantity and quality of the OM is also used to reconstruct the paleoenvironmental conditions since they are the result of the combined influence of the biomass productivity, biochemical degradation, and of the OM depositional processes (e.g., Mendonça Fihlo et al., 2012).

The marls and mudstones of the LI of BORI are characterized by the highest concentration of TOC together with high absolute values and enrichment factors of Mo, U, V, Ni, and Cu (Fig. 8C and 11A). The enrichment in Mo, U, and V combined with the good correlation observed between the RSTE and the TOC content, suggests overall anoxic, and probably euxinic, sea bottom conditions during the accumulation of the LI sediments (e.g., Tribovillard et al., 2006). Anoxic sea bottom conditions are well documented in the diagrams (Fig. 11B and C) of Algeo and Tribovillard (2009) and Piper and Calvert (2009). The Mo vs U EF diagram suggests that at least some contribution of Mo is related with the particulate shuttle effect (Algeo and Tribovillard, 2009, Fig. 11B). This effect has also been proposed as an effective mechanism of Mo enrichment in the lowermost organic-rich stratigraphic level ("*cocina*") of the VMFm (Krim et al., 2019; Spalletti et al., 2019; Capelli et al., 2020). In spite of the particulate shuttle effect, the high enrichment of V reported in the LI suggests that the sea bottom was indeed a reducing environment. This is in agreement with the very high TOC

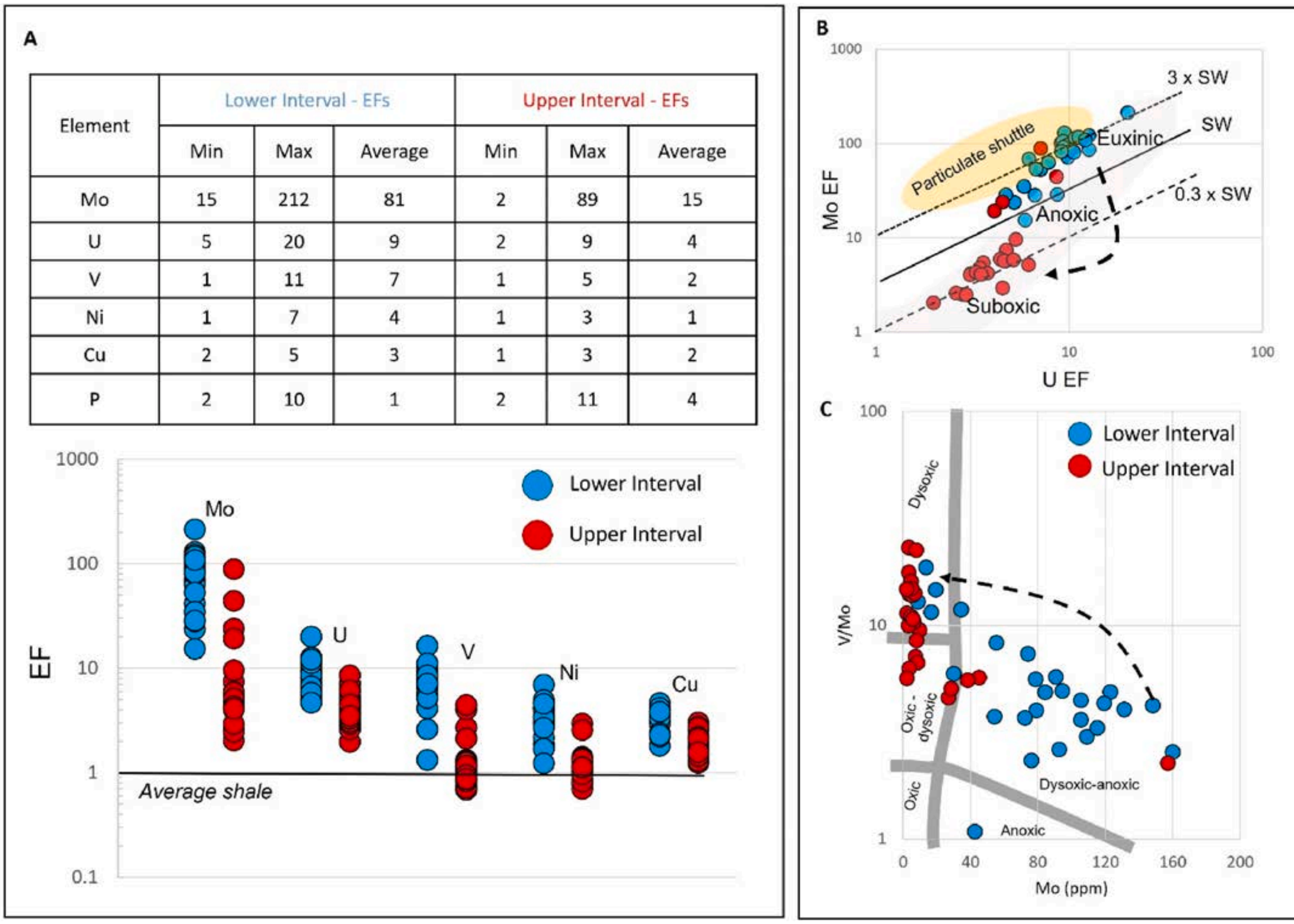

Element	Lower Interval - EFs			Upper Interval - EFs		
	Min	Max	Average	Min	Max	Average
Mo	15	212	81	2	89	15
U	5	20	9	2	9	4
V	1	11	7	1	5	2
Ni	1	7	4	1	3	1
Cu	2	5	3	1	3	2
P	2	10	1	2	11	4

Fig. 11. **A**) Enrichment factors (EFs) of the redox sensitive trace elements of the LI and UI of the BORI in the Puerta Curaco section compared against the average shale composition. **B**) Mo vs U EFs diagram from Algeo and Tribovillard (2009). **C**) V/Mo vs Mo (ppm) diagram of Piper and Calvert (2009).

content, preservation of fine, delicate lamination in the sediments, and abundant AOM content (Figs. 9 and 10A), the latter being the result of preservation of autochthonous planktonic OM in reducing sea bottoms (Summerhayes, 1987; Tyson, 1989) like those developed in the distal carbonate ramps of VMFm (Fig. 12A). P values are relatively low throughout the entire studied interval ($<$0.3 wt%), although the P/Al ratio shows higher values than the AS throughout the entire BORI (Fig. 8C). In deep marine environments, P is mainly sourced to the sea bottom by dead phytoplankton. Afterwards, under anoxic conditions, P is generally released back into the water column, enhancing productivity (Tribovillard et al., 2006). Therefore, the relatively low values of P in the marls and mudstones of the VMFm may reflect strong anoxic conditions in the sea bottom. Nevertheless, some of the primary P was retained in the sediments as authigenic fluorapatite (Fig. 7) suggesting very high initial concentrations of P (e.g., Tribovillard et al., 2006) associated to a high productivity in the water column. Ni and Cu enrichment in the LI of the BORI together with the accumulation of radiolarian-rich facies and the documented Si_{excess} (Fig. 11A and 12A) also point to high productivity. Therefore, the high productivity of the sea water may have been one of the main causes for the overall anoxic sea bottom conditions reported in the LI of the BORI, because the accumulation of dead biomass contributed to the full consumption of oxygen (e.g., Pedersen and Calvert, 1990; Tribovillard et al., 2006, Fig. 12A).

The UI is characterized by a reduction of the absolute values of RSTE and TOC, suggesting a change towards more oxygenated conditions at the sea bottom and in the pore waters immediately below, consistently with the presence of bioturbated marls and limestones (Fig. 2F, 4H and 11B and C). A sharp reduction of the paleoproductivity proxies is also observed in the UI (Fig. 11A), in agreement with the reduction of radiolarian-rich facies and AOM content, suggesting a link between productivity and oxygenation of the sea bottom. The reduction of the productivity in the water column during the accumulation of the UI led to less OM accumulation and less oxygen consumption at the sea bottom (Fig. 12B).

The high TOC and RSTE contents at the LI of the BORI occurred in a general transgressive pattern (Domínguez et al., 2020), suggesting that high productivity, and associated anoxic conditions at the sea bottom, are related to the Berriasian marine transgression (Fig. 12A). A marine transgression may enhance marine OM accumulation in basinal settings by two processes: 1) an increase of the stratification of the water column and 2) a reduction of the clastic input due to landward migration of the shoreface (e.g., Wignall, 1991; Arthur and Sageman, 2005). The deepening of the water column decreases bottom-water ventilation, enhances anoxia in the sea bottom and favors the preservation of OM (Arthur and Sageman, 2005). The stratification of the water column of the Neuquén Basin during transgressive systems tracts of the VMFm is also supported by the presence of microbial bindstones (Legarreta and Uliana, 1991, Fig. 2E and 4A) presumably formed under conditions of high OM supply and low sediment input (Kietzmann et al., 2016). Interestingly, the lowermost analyzed marl (254.74 m) gave a relatively high $\delta^{13}C_{org}$ value ($-$25.8‰) compared to the other BORI samples. This ^{13}C enrichment is not associated with a high input of terrestrial OM (Fig. 9) and might be a consequence of isotopic fractionation by cyanobacteria (e.g., Carpenter

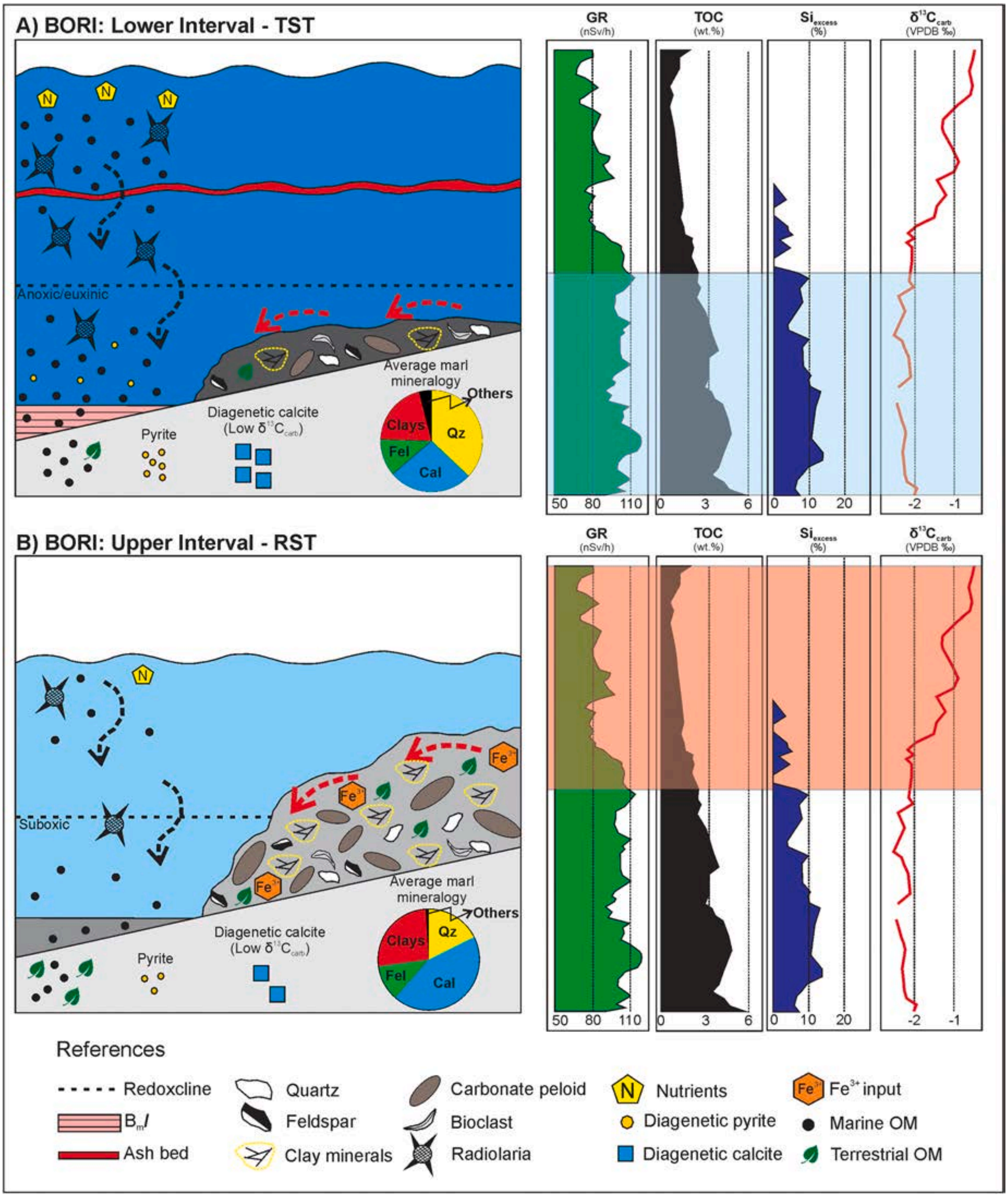

Fig. 12. Paleoenvironmental reconstruction of the Lower and Upper Interval of the BORI indicating the main mineralogical and geochemical features of the rock. **A)** Paleoenvironmental reconstruction of the Lower Interval (transgressive systems tract) characterized by a sea level rise, anoxic/euxinic conditions in the sea bottom and high productivity in the water column. This resulted in the increased accumulation of mostly marine OM, which resulted in high values of Total Gamma Ray, TOC, Si_{excess}, and relatively low values of $\delta^{13}C_{carb}$. B) Paleoenvironmental reconstruction of the Upper Interval (regressive systems tract) characterized by a relative sea level fall, suboxic conditions in the sea bottom and relatively low productivity in the water column. This resulted in relatively low content of OM, increase in the input of terrestrial OM, low values of TGR, TOC, lack of Si_{excess}, and relatively high values of $\delta^{13}C_{carb}$. For further explanations see the text.

et al., 1997; Saelen et al., 2000) in a general context of sea water stratification during the early times of the marine transgression. Additional geochemical studies are needed to confirm this.

As in the basal LI of the BORI, many organic-rich intervals of the VMFm are located within transgressive systems tracts (Kietzmann et al., 2016; Domínguez et al., 2020; Rodriguez Blanco et al., 2022a). Nonetheless, not all the transgressive systems tracts of the VMFm are characterized by high TOC content (Kietzmann et al., 2016; Capelli et al., 2020; Rodriguez Blanco et al., 2020; Domínguez et al., 2020), suggesting other factors, besides marine transgressions, intervene in the formation of OM-rich intervals of the unit. The productivity proxies (Ni, Cu, Si_{excess}), indicate an increased availability of nutrients in the sea water during the accumulation of the LI. Two sources of nutrients are generally proposed to explain increasing productivity: an external source due to a change towards more humid conditions in the continent (e.g., Hallock and Schlager, 1986; Föllmi, 1995) or an internal source due to the input of deoxygenated and phosphate-rich water (e.g., Arthur and Sageman, 2005). A change towards more humid conditions in the Berriasian has been proposed (Capelli et al., 2020; Capelli, 2021) on the basis of geochemical and clay mineral analyses of the VMFm. The fact that kaolinite is present in the 2–16 μm size fraction of the LI may be indicative of a more humid climate in the hinterlands during the early Late Berriasian. This climatic change seems to be a global process, since a change towards more humid conditions in the middle to upper Berriasian have been proposed for the Tethyan, Atlantic Ocean and Russian platforms realms (Hallam, 1984; Schnyder et al., 2005, 2006; Morales et al., 2013, 2016). The early Late Berriasian age of the BORI of the VMFm is therefore consistent with a worldwide paleoclimatic change towards more humid conditions. The paleoclimatic change enhanced nutrient supply to the sea, triggering outstanding productivity in the water column of the Neuquén Basin.

The good correlation between the RSTE, the TOC content and the microfacies analyses in the BORI suggests that these proxies may be reliable indicators of past ocean oxygenation and productivity in deeply buried successions of the VMFm.

5.3. Linking sequence stratigraphy and cyclicity with the mineralogy and geochemistry of the BORI

Previous sequence stratigraphic studies of the VMFm have shown specific lithological patterns associated with the different systems tracts represented in the unit (Spalletti et al., 2000; Kietzmann et al., 2014, 2016; Zeller et al., 2015; Rodriguez Blanco et al., 2020, 2022a). In both, composite sequences (CSs) and high-frequency sequences (HFSs), transgressive systems tracts (TSTs) are mostly constituted of marls and mudstones with high TOC content, whereas regressive system tracts (RSTs) are generally constituted of marls, calcareous marls, and limestones with relatively low TOC content (Kietzmann et al., 2014, 2016; Zeller et al., 2015). A similar trend is recorded in the BORI of Puerta Curaco section, where the LI is less calcareous and richer in TOC and the opposite is observed in the UI suggesting that these mineralogical and geochemical trends are related with sea level changes. Considering the reported trends, thickness, and stratigraphic position of the analyzed section, the LI and UI are likely the TST and RST of HFS 11, at the base of CS 4, in the sequence stratigraphic scheme proposed in Kietzmann et al. (2016). Based on preliminary cyclostratigraphic data (Kohan Martinez, 2022) and the biostratigraphic data presented in this work, the average sedimentation rate for the BORI is 14 m/Ma. Nevertheless, the estimated sedimentation rate in the TST is ~10 m/Ma, while in the RST is ~30 m/Ma. These sedimentation rates are consistent with those previously proposed by the authors for basinal and distal outer ramp facies (e.g., Kietzmann et al., 2014, 2016, 2021b).

The petrography and geochemistry of the LI reveals that the TST is characterized by a high content of quartz, mostly of non-detrital origin, high TGR values, high Mo, U, V, Ni and Cu enrichment, relatively low $\delta^{13}C_{carb}$ values (−3 to −2‰), high TOC and AOM of marine origin. The high TOC content of the LI responds not only to high productivity in the water column and overall anoxic conditions at the sea bottom, but also to the relative low sedimentation rate which prevented high OM dilution (e.g., Gautier et al., 1984; Stein, 1986). This is in agreement with the relatively low clay mineral and phytoclast content which indicates minor detrital input (Figs. 9, 11A and 12A).

On the other hand, the UI represents a RST characterized by an increase of calcite and clay minerals, lower TGR values, low Mo, U, V, Ni and Cu enrichment, higher $\delta^{13}C_{carb}$ values (−1 to 0‰), low TOC and higher content of terrestrial phytoclasts, in agreement with the higher sedimentation rate estimated for the RST (Figs. 9, 11A and 12B). The increase of clay minerals in the UI is not only supported by the XRD analyses, but also by the increment on the absolute content of Al and K (Figs. 7 and 8A). The increment of calcite in the UI is clearly evidenced by the increase on the average content of Ca (17.34 wt%) and Mn (0.05 wt%) in the UI compared to respective average values of 12.42 wt% and 0.03 wt% in the LI (Fig. 8B). The increase of calcite, clay minerals, and phytoclasts may be associated with a general decrease of the accommodation space in the basin, resulting in a general progradation of the carbonate ramp with peloidal-rich facies (Kietzmann et al., 2016). The increase of clay minerals indicates that both, carbonate and clays were exported together, probably in the form of mixed micrite/clay peloids (e.g., Wagreich and Koukal, 2019, Fig. 4G). The general increase of the phytoclast content in the UI suggests an increment of terrestrial input and confronts previous studies that proposed a uniform marine origin for the OM of the VMFm, with negligible contribution of terrestrial OM and stratigraphic variations basinwide (e.g., Brisson et al., 2020). Our palynological analyses indicate abundant large, blade-shaped, opaque phytoclasts, supporting a transitional/terrestrial provenance (Steffen and Gorin, 1993; Götz et al., 2005, Fig. 10B and C), for the OM of the BORI, especially in the UI (Fig. 9). Opaque phytoclasts transported to distal marine settings by storms or turbidity currents may have been either derived from the oxidation of translucent woody material reworked from estuarine and deltaic environments (Tyson, 1993; Ercegovac and Kostic, 2006; Carvalho et al., 2006; Otharán et al., 2022), or by the oxidation of terrestrial OM after deposition (e.g., Tyson, 1993; Ercegovac and Kostic, 2006). The abundance of peloids and intraclasts in the marls of the UI contrast with the radiolarian abundance in the wackestones of the LI, supporting deposition in a shallower marine environment for the UI (Kietzmann et al., 2014, 2016, 2020; Catalano et al., 2018; Minisini et al., 2020b; Rodriguez Blanco et al., 2022a). In addition, the $\delta^{13}C_{carb}$ values of the UI are higher than those reported in the LI and closer to the "normal" isotopic composition of calcite precipitated in the Berriasian marine waters (Weissert and Erba, 2004; Katz et al., 2005; Gómez Dacal et al., 2018). This suggests that calcite of the UI was mostly sourced in the form of primary carbonatic components (e.g., bioclasts, micritic peloids, intraclasts) with less diagenetic contribution (Scasso et al., 2002; Catalano et al., 2018; Rodriguez Blanco et al., 2018). Peloids were probably first sedimented near the coast and later resuspended and exported to distal settings by storms and their associated basinward currents and flows (e.g., Huggett et al., 2015; Kietzmann et al., 2016). A basinwide increment in the terrestrial input during the late Berriasian would explain the increment of phytoclasts and Fe-rich chlorite in the UI of the BORI, which took place in the context of the progressive transition from a carbonate ramp (VMFm) to a shallow marine, mixed siliciclastic/carbonate environment (Quintuco Fm) (Kietzmann et al., 2016, 2018a; Capelli et al., 2018, 2020).

The content of plagioclase is relatively constant throughout the entire BORI, averaging 11 and 10 wt% in the LI and UI respectively (Fig. 7), in good agreement with the absolute content of Na (Fig. 8A). The decrease of the Na/Al ratio in the UI results from the relative increase on the clay mineral content. The lowermost 3 m of the UI presents the highest values of plagioclase (25 wt%; Fig. 7) and is highlighted by the Sr/Ca ratio, which is markedly higher than in the rest of the BORI (Fig. 8B). Therefore the Sr in the marls and mudstones is not only associated with carbonates, as in the rest of the BORI, but it is also related to the abundance of feldspar (e.g., Lerouge et al., 2010). As plagioclase is common in the argilized ash beds of the VMFm (Rutman et al., 2021) the high content of Sr in this interval, macroscopically characterized by the abundance of ash beds (Fig. 3), is related to the plagioclase from millimetric volcanic ash beds into the marls and mudstones of the BORI. Therefore, the mineralogy of the marls and mudstones of the BORI is not only a consequence of the productivity of the water column and sea level changes, but it also reflects periods of enhanced volcanic input. Considering this, the Sr/Ca ratio can be used as a proxy to track the presence of volcanism in marls and mudstones of the VMFm.

Four ~ 5–10 m thick cycles, are recognized in the BORI on the basis of the Th/K, Th/U ratios, TOC content and, to a lesser extent, on the relative abundance of AOM and phytoclasts (Figs. 6 and 9). These higher frequency cycles are nested in the same stratigraphic interval than the LI-UI cycle and they are better expressed in the LI (Fig. 6). They are characterized by a gradual increase of the Th/U and Th/K ratios, and a gradual decrease of the TOC content with a relative increase of AOM, towards the top of each cycle. On the basis of their thickness and the average sedimentation rate of the VMFm (Kietzmann et al., 2014, 2015) an approximated duration of 240–500 kyr can be calculated for each high-frequency cycle, that lies within the Milankovitch frequency band. According to the astronomical time scale built for the Tithonian-Berriasian of the Neuquén Basin (Kietzmann et al., 2018b), the studied interval contains seven low frequency eccentricity cycles (E) of the Earth's orbit, which would be consistent with the cyclical variations observed in our data. The high Th/K ratio may reflect more humid climates in the hinterlands, where an increase of weathering resulted in the formation of clay minerals with high Th/K ratio (e.g., Schnyder et al., 2006; Hesselbo et al., 2009). The more humid climatic episodes corresponding to C1–C3 cycles of the LI together with the presence of kaolinite in the 2–16 μm size fraction of the LI support a more humid climate during the deposition of the LI. This high-frequency, cyclic paleoclimatic changes towards more humid conditions can be interpreted in the same way as the LI-UI cycle, with more humid climates and higher runoffs in the hinterlands leading to an increase of available nutrients into the sea and proliferation of productivity in the water column (e.g., Föllmi, 1995).

5.4. Insights in the characterization of the BORI as a sweet spot

The 50-m thick BORI has the typical thickness of the organic-rich stratigraphic intervals of the VMFm and may be regarded as an attractive interval for unconventional hydrocarbon production in the northern blocks of the basin (Fantin et al., 2014; Desjardins et al., 2016; Lanusse Noguera et al., 2017; Domínguez et al., 2020; Ponce et al., 2022). In these unconventional hydrocarbon prospects, the study of the mineralogy and geochemistry is crucial since they have direct influence in the petrophysics and geomechanics of the reservoirs (e.g., Jarvie et al., 2007; Peltonen et al., 2009; Wilson et al., 2016; Milliken and Olson, 2017; Dong et al., 2018; Liu et al., 2020; Ortiz et al., 2020). Considering this, at least four aspects should be taken into consideration when analyzing the BORI as a possible stratigraphic interval for unconventional hydrocarbon production in the VMFm: 1) the TOC distribution, 2) the bulk mineralogy, 3) the type of quartz, and 4) the clay mineralogy, since these features may enhance or reduce the production of hydrocarbons (e.g., Milliken and Olson, 2017; Yi-Kai et al., 2017; Dong et al., 2018; Liu et al., 2020; Ortiz et al., 2020).

The markedly higher TOC content in the LI (4.2 wt% on average) compared to the UI (1.5 wt% on average; Fig. 12) makes the LI more attractive than the UI for hydrocarbon production. Additionally, the porosity in the VMFm is mainly organic porosity (Crousse et al., 2015; Ortiz et al., 2020; Spacapan et al., 2021) and higher contents of OM will result in higher porosities.

A bulk mineralogy with higher content of quartz, calcite, and feldspar enhances the brittleness of unconventional hydrocarbon reservoirs and favors reservoir stimulation by hydraulic fracturing. The opposite is true for high clay mineral and OM content (Jarvie et al., 2007; Rickman et al., 2008; Wang and Gale, 2009; Rybacki et al., 2016; Dong et al., 2018; Liu et al., 2020; Varela et al., 2020). The average bulk clay mineral content is generally lower than 40 wt% in the VMFm. This value is usually set as a cut off value when assessing reservoir's fracability (Varela et al., 2020). Both intervals of the BORI are well below the cut off, but the average content of "brittle" minerals is slightly higher in the LI (quartz + calcite + feldspar = 76 wt%, Brittle index = 0.44 ± 0.10) than in the UI (quartz + calcite + feldspar = 73 wt%, Brittle index = 0.20 ± 0.11). The opposite is true for the bulk clay mineral content, which averages 21 wt% in the LI and 26 wt% in the UI (Fig. 12). In addition, the average content of quartz is markedly higher in the LI (37 wt%) than in the UI (18 wt%), also indicating than the LI is more brittle than the UI and so, that the LI will be better for reservoir's stimulation by hydraulic fracturing.

The type of quartz is also important for the reservoir's geomechanics, since in mudstones biogenic quartz is usually pervasively distributed in the rock as authigenic microcrystals, whereas detrital quartz is usually distributed as isolated grains (Milliken and Olson, 2017; Dong et al., 2018; Liu et al., 2020). The pervasive distribution of quartz increase reservoir's brittleness by favoring the development of a rigid network (e.g., Dong et al., 2018). The Si_{excess} in the LI of the BORI (Fig. 8A and 12A) is sourced by the radiolarians in the radiolarian-bearing mudstones and marls, a common lithology in the VMFm (Scasso et al., 2002; Kietzmann et al., 2014, 2016; Catalano et al., 2018; Capelli et al., 2018, 2020; Milliken et al., 2019) associated with high-productivity stages of the water column (see section 5.2). The early filling of the radiolarian tests with calcite as well as the replacement of their silica skeletons by calcite and chlorite during diagenesis, led to the massive precipitation of euhedral microcrystals of quartz in the matrix. This process has been well documented in the studied section of Puerta Curaco (Catalano et al., 2018) and in the nearby El Trapial block (Milliken et al., 2019, Fig. 1) and extended to the entire basin in both outcrop and subsurface blocks (e.g., Kietzmann et al., 2020). Another potential source of Si that may have led to the precipitation of quartz in the matrix is the transformation of smectite to illite (e.g., Hower et al., 1976). In the BORI, I/S contribution to the <2 μm size fraction is subtly higher in the LI than in the UI and this trend is even more evident in the 2–16 μm size fraction (Fig. 7). The higher content of I/S in the LI may have contributed to the higher amounts of quartz reported in the LI, and so to enhance reservoir's brittleness.

The predominance of I/S, formed by smectite transformation through burial, may have favored the generation of hydrocarbons, especially in the LI of the BORI where the I/S is more abundant (Fig. 7). Smectite was the main clay mineral present in the rocks when the OM was immature. Compared to other clay minerals like chlorite or illite, smectite has a larger specific surface, which results in higher quantities of adsorbed OM in both the external surface and the interlayer space (e.g., Theng, 1979; Hillier, 1995; Cai et al., 2022; Zhao et al., 2023). During burial, OM is cracked to produce hydrocarbons, leading to the formation of organic pores (Yi-Kai et al., 2017). Therefore, compared to other clay minerals like illite or chlorite, a relatively high initial content of smectite will favor the adsorption of OM, which during burial should favor the development of organic porosity in the VMFm. Furthermore, the size of the organic pores in the VMFm correlates positively with the thermal maturity of the OM and sections submitted to a high diagenetic grade, like the studied section, have larger organic pores (Kietzmann et al., 2020). In addition, the transformation of smectite to I/S releases interlayered water, which may result in the formation of intercrystalline pores, thus increasing the secondary porosity in both matrix and OM (Yi-Kai et al., 2017). Therefore, the presence of primary smectite in the BORI may favor unconventional hydrocarbon production in two ways: 1) by increasing the quantities of adsorbed OM resulting in higher TOC values and more organic pores and 2) by the formation of intercrystalline pores due to the release of interlayered water during the transformation of smectite to I/S.

Summarizing, the TOC content, bulk mineralogy, type of quartz, and clay mineralogy of the BORI in general, and especially in the LI, result truly attractive for future unconventional hydrocarbon production of this organic-rich stratigraphic interval in the VMFm.

6. Conclusions

The multiproxy analysis (petrography, mineralogy and geochemistry) of the BORI allowed an unprecedented, comprehensive analysis of its paleoenvironmental and sequence stratigraphic framework. This study confirms, refines and clarifies previous assumptions and establishes new criteria applicable for other organic-rich intervals of the VMFm in the Neuquén Basin.

The BORI is 50 m-thick in the Puerta Curaco section and presents a late Early to early Late Berriasian age, comprising the upper *Calpionella* and lower *Calpionellopsis* calpionellids Zones and the *Stomiosphaera wanneri* calcisphere Zone. The OM thermal maturity reached the dry gas window stage, in agreement with the high-grade diagenetic mineralogy of the marls and mudstones, mostly constituted by high-ordered I/S, chlorite, illite, albite, calcite and quartz. The combination of the mineralogical and ME analyses allowed to use the Sr/Ca and Mg/Al ratios as proxies to track the presence of diluted volcanic material and dolomite in relatively homogenous fine-grained successions of the VMFm.

The LI of the BORI is mostly characterized by radiolarian-rich marls, higher TOC and quartz content. The paleoenvironmental reconstruction suggests high productivity in the water column and overall anoxic conditions at the sea bottom, which favored the accumulation and preservation of OM. The relatively low $\delta^{13}C_{carb}$ values of the calcite indicate a significative diagenetic contribution from aqueous CO_2 formed after oxidation of the OM. The UI is mostly composed of carbonate and clay peloidal facies, with lower TOC and higher calcite content, whereas the geochemical analyses indicated low productivity in the water column and a more oxygenated sea bottom. The relatively higher $\delta^{13}C_{carb}$ values suggest less diagenetic contribution of CO_2 from OM oxidation.

The palynofacies study revealed an unexpected significant terrestrial contribution for the VMFm, which is normally assumed to exclusively have marine OM. This palynofacies conformation is related to the progressive progradation of the shallow marine environment of the Quintuco Fm.

The overall anoxic conditions of the sea bottom during the accumulation of the LI were reached by the combined effects of sea water stratification caused by the Berriasian transgression and the high productivity of the water column. The latter is attributed to the worldwide paleoclimate change towards more humid conditions reported in the early Late Berriasian, which should have increased continental runoff and nutrient supply to the ocean, triggering productivity of the water column in the Neuquén Basin. In addition, higher frequency, humid/arid cycles (~5–10 m thick) recorded in the Th/K ratio may reflect 240–500 kyr cycles related with the Earth orbital's eccentricity cycles.

The combination of the prevailing environmental conditions during sedimentation and the diagenetic history makes the BORI of the VMFm a highly attractive target for unconventional hydrocarbon production. This is especially remarkable in the LI, richer in OM and with abundant brittle minerals and Si_{excess} that enhance reservoir's fracability.

CRediT authorship contribution statement

Ignacio A. Capelli: Writing – review & editing, Writing – original draft, Methodology, Investigation, Conceptualization. **Roberto A. Scasso:** Writing – review & editing, Writing – original draft, Resources, Project administration, Methodology, Investigation, Funding acquisition, Conceptualization. **Jorge E. Spangenberg:** Writing – review & editing, Writing – original draft, Resources, Methodology, Investigation, Funding acquisition, Conceptualization. **Diego A. Kietzmann:** Writing – review & editing, Writing – original draft, Resources, Project administration, Methodology, Investigation, Funding acquisition, Conceptualization. **Mercedes Prámparo:** Writing – review & editing, Writing – original draft, Resources, Methodology, Investigation, Conceptualization. **Thierry Adatte:** Writing – review & editing, Writing – original draft, Resources, Project administration, Methodology, Investigation, Funding acquisition, Conceptualization.

Declaration of competing interest

The authors declare that they have no known competing financial interests or personal relationships that could have appeared to influence the work reported in this paper.

Data availability

Data will be made available on request.

Acknowledgments

The present contribution is part of the PhD thesis of the first author. Financial support was provided by the National Council of Scientific and Technical Research of Argentina (CONICET) and by the Vaca Muerta Consortium integrated by the University of Buenos Aires and the oil companies Shell, Chevron and Total and we would like to acknowledge the companies for allowing the publication of the results. CONICET and the Swiss Government granted the PhD of Ignacio Capelli and the International Association of Sedimentologists (IAS) provided him a postgraduate research grant. We acknowledge Oliver Reubi and Tiffany Monnier (University of Lausanne) for their assistance in the lab and the XRF measurements and Cecilia Genazzini and Martin Morosi (CETMIC) for their assistance in the lab. We also thank Daniel Minisini (Shell) for his help regarding Spectral Gamma-Ray measurements and field discussions and Alejandro Bande (Tecpetrol) and Fernanda Cravero (CETMIC) for a critical review and corrections of an earlier version of the manuscript. We acknowledge three anonymous reviewers for their constructive corrections and comments, which contributed significantly to improve the manuscript and Professor Daniel Alessi for editorial handling. We specially want to acknowledge Prof. Karl Föllmi, who unfortunately passed away during the realization of this research. Karl was an outstanding colleague, both scientifically and humanly. An honest and passionate geologist with a kind and persuasive way to share his ideas.

Appendix A. Supplementary data

Supplementary data to this article can be found online at https://doi.org/10.1016/j.marpetgeo.2024.106760.

References

Adatte, T., Stinnesbeck, W., Keller, G., 1996. Lithostratigraphic and mineralogic correlations of near K/T boundary clastic sediments in northeastern Mexico: implications for origin and nature of deposition. Spec. Pap. Geol. Soc. Am. 307 (January), 211–226. https://doi.org/10.1130/0-8137-2307-8.211.

Algeo, T.J., Maynard, J.B., 2004. Trace-element behavior and redox facies in core shales of Upper Pennsylvanian Kansas-type cyclothems. Chem. Geol. 206, 289–318. https://doi.org/10.1016/j.chemgeo.2003.12.009.

Algeo, T.J., Tribovillard, N., 2009. Environmental analysis of paleoceanographic systems based on molybdenum-uranium covariation. Chem. Geol. 268, 211–225.

Arthur, M.A., Sageman, B.B., 2005. Sea-Level control on source-rock development: perspectives from the holocene black Sea, the mid-cretaceous western interior basin of north America, and the late devonian appalachian basin. In: Harris, N.B. (Ed.), The Deposition of Orvanic-Rcarbon-Rich Sediments: Models, Mechanisms, and Consequences. SEPM Spécial Pblication.

Askenazi, A., Biscayart, P., Cáneva, M., Montenegro, S., 2013. Analogía entre la Formación Vaca Muerta y Shale Gas/Oil Plays de EEUU. Soc. Pet. Eng. 20.

Baker, J.C., Havord, P.J., Martin, K.R., Ameed, K., Ghori, R., 2000. Diagenesis and petrophysics of the early permian moogooloo sandstone, southern carnarvon basin, western Australia 1. AAPG (Am. Assoc. Pet. Geol.) Bull. 84 (2). https://pubs.geoscienceworld.org/aapgbull/article-pdf/84/2/250/3357313/250.pdf.

Batten, D.J., 1996. Palynofacies and palaeoenvironmental interpretation. In: Jansonius, J., McGregor, D.C. (Eds.), Palynology: Principles and Applications, vol. 3. American Association of Stratigraphic Palynologists Foundation, College Station, TX, pp. 1011–1064.

Beaufort, D., Rigault, C., Billon, S., Billault, V., Inoue, A., Inoue, S., Patrier, P., 2015. Chlorite and chloritization processes through mixed-layer mineral series in low-temperature geological systems – a review. Clay Miner. 50, 497–523. https://doi.org/10.1180/claymin.2015.050.4.06.

Behar, F., Beaumont, V., De, B., Penteado, H.L., 2001. Rock-eval 6 technology: performances and developments. Oil Gas Sci. Technol. 56, 111–134. https://doi.org/10.2516/ogst:2001013.

Boles, J.R., 1982. Active albitization of plagioclase, gulf coast tertiary. Am. J. Sci. 282, 165–180. https://doi.org/10.2475/ajs.282.2.165.

Boles, J.R., Franks, S.G., 1979. Clay diagenesis in wilcox sandstones of southwest Texas: implications of smectite diagenesis on sandstone cementation. SEPM J. Sediment. Res. 49, 55–70.

Brisson, I.E., Fasola, M.E., Villar, H.J., 2020. Organic geochemical patterns of the vaca Muerta Formation. In: En, Minisini, D., Fantin, M., Lanusse Noguera, I., Leanza, H.

(Eds.), Integrated Geology of Unconventionals: the Case of the Vaca Muerta Play, Argentina, vol. 121. AAPG Memoir, pp. 297–328. https://doi.org/10.1306/13682231M1203834, 121.

Cai, J., Du, J., Song, M., Lei, T., Wang, X., L, Y., 2022. Control of clay mineral properties on hydrocarbon generation of organo-clay complexes: evidence from high-temperature pyrolysis experiments. Appl. Clay Sci. 216, 106368.

Calvert, S.E., Pedersen, T.F., 1993. Geochemistry of Recent oxic and anoxic marine sediments: implications for the geological record. Mar. Geol. 113, 67–88. https://doi.org/10.1016/0025-3227(93)90150-T.

Calvert, S.E., Pedersen, T.F., 2007. Elemental proxies for palaeoclimatic and palaeoceanographic variability in marine sediments: interpretation and application. Dev. Mar. Geol. 1, 567–644. https://doi.org/10.1016/S1572-5480(07)01019-6.

Capelli, I.A., 2021. Estudio de la mineralogía y geoquímica del Sistema Vaca Muerta-Quintuco (Tithoniano-Valanginiano) de la Cuenca Neuquina y su implicancia en las reconstrucciones paleoambientales, paleooclimáticas y diagenéticas. PhD. Thesis. Universidad de Buenos Aires, Buenos Aires, p. 301.

Capelli, I.A., Scasso, R.A., Kietzmann, D.A., Cravero, F., Minisini, D., Catalano, J.P., 2018. Mineralogical and geochemical trends of the vaca muerta-quintuco system in the Puerta Curaco section, Neuquén Basin. Rev. Asoc. Geol. Argent. 75 (2), 210–228.

Capelli, I.A., Scasso, R.A., Spangenberg, J.E., Kietzmann, D.A., Cravero, F., Duperron, M., Adatte, T., 2020. Mineralogy and geochemistry of deeply-buried marine sediments of the Vaca Muerta-Quintuco system in the Neuquén Basin (Chacay Melehue section), Argentina: paleoclimatic and paleoenvironmental implications for the global Tithonian-Valanginian reconstructions. J. South Am. Earth Sci. 107, 103103 https://doi.org/10.1016/j.jsames.2020.103103.

Capelli, I.A., Scasso, R.A., Cravero, F., Kietzmann, D.A., Vallejo, D., Adatte, T., 2021. Late-diagenetic clay mineral assemblages in carbonatized ash beds of the Vaca Muerta Formation (Neuquén Basin, Argentina): insights into the diagenetic formation of chlorite. Mar. Petrol. Geol. 132, 105207 https://doi.org/10.1016/j.marpetgeo.2021.105207.

Carpenter, E.J., Harvey, H.R., Fryi, B., Capone, D.G., 1997. Biogeochemical tracers of the marine cyanobacterium Trichodesmium. Deep-Sea Res. 44 (1), 27–38. https://doi.org/10.1016/S0967-0637(96)00091-X.

Carvalho, M. de A., Mendonça Filho, J.G., Menezes, T.R., 2006. Paleoenvironmental reconstruction based on palynofacies analysis of the aptian–albian succession of the sergipe basin, northeastern Brazil. Mar. Micropaleontol. 59, 56–81.

Catalano, J.P., Scasso, R.A., Kietzmann, D., Föllmi, K., Spangenberg, J., Capelli, I.A., 2018. Carbonate Sedimentology and Diagenesis of the Vaca Muerta Formation at Puerta Curaco, Neuquén Basin, Argentina. X Congreso de Exploración y Desarrollo de Hidrocarburos, Argentina, pp. 481–501.

Chamley, H., 1989. Clay Sedimentology. Springer-Verlag Berlin Heidelberg, p. 623.

Crousse, L., Cuervo, S., Vallejo, D., Laurent, M., Fischer, T., McCarty, D., 2015. Unconventional shale pore system characterization in El Trapial area, Vaca Muerta, Argentina. In: Society of Petroleum Engineers - Unconventional Resources Technology Conference, URTeC 2015, vol. 2012. https://doi.org/10.2118/178596-ms.

Desjardins, P., Fantin, M., González Tomassini, F., Reijenstein, H., Sattler, F., Domínguez, F., Kietzmann, D., Leanza, H., Bande, A., Benoit, S., Borgnia, M., Vittore, F., Simo, T., Minisini, D., 2016. Estratigrafía sísmica regional. In: González, G., Vallejo, M.D., Kietzmann, D., Marchal, D., Desjardins, P., González Tomassini, F., Gómez Rivarola, L., Domínguez, R.F., Fantin, M. (Eds.), Transecta Regional de la Formación Vaca Muerta: integración de sísmica, registros de pozos, coronas y afloramientos. Instituto Argentino del Gas y Petróleo, Buenos Aires, pp. 5–22.

de Barrio, A., Ferraresi, P., Köhler, G., Marchal, D., Blanco, S., 2018. Estudio comparativo de testigos corona de las dos secciones enriquecidas de la Formación Vaca Muerta en la zona de shale gas, noroeste del engolfamiento Neuquino. Rev. la Asoc. Geol. Argentina 75, 23–30.

Dickson, J., 1965. A modified technique for carbonates in thin section. Nature 205, 587.

DÓdorico, A.A., 2009. Estratigrafía y petrología de la Fm. Vaca Muerta. Perfil de Puerta Curaco. Provincia del Neuquén. Trabajo Final de Licenciatura, Universidad de Buenos Aires (inédito), Buenos Aires, p. 159.

Doebelin, N., Kleeberg, R., 2015. Profex: a graphical user interface for the Rietveld refinement program BGMN. J. Appl. Crystallogr. 48 (September), 1573–1580. https://doi.org/10.1107/S1600576715014685.

Domínguez, F.R., Lanusse Noguera, I., Continanzia, M.J., Mykietiuk, J., Ponce, C., Pérez, G., Guerello, R., Caneva, M., Di Benedetto, M., Catuneanu, O., Cristallini, E., 2016. Organic-rich stratigraphic units in the Vaca Muerta formation, and their distribution and characterization in the Neuquén Basin (Argentina). In: SPE/AAPG/SEG Unconv. Resour. Technol. Conf. 2016. https://doi.org/10.15530/urtec-2016-2456851.

Domínguez, F.R., Catuneanu, O., Reienstein, H.M., Notta, R., Posamentier, H.W., 2020. Sequence stratigraphy and the three-dimensional distribution of organic-rich units. In: Minisini, D., Fantin, M., Lanusse Noguera, I., Leanza, H. (Eds.), Integrated Geology of Unconventionals: the Case of the Vaca Muerta Play, Argentina, vol. 121. AAPG Memoir, pp. 163–200. https://doi.org/10.1306/13682221M1203264.

Dong, T., Harris, N.B., Knapp, L.J., McMillan, J.M., Bish, D.L., 2018. The effect of thermal maturity on geomechanical properties in shale reservoirs: an example from the Upper Devonian Duvernay Formation, Western Canada Sedimentary Basin. Mar. Petrol. Geol. 97, 137–153. https://doi.org/10.1016/j.marpetgeo.2018.07.007.

Dunoyer de Segonzac, G., 1970. The transformation of clay minerals during diagenesis and low-grade metamorphism: a review. Sedimentology 15, 281–346. https://doi.org/10.1111/j.1365-3091.1970.tb02190.x.

Ehrenberg, S.N., 1993. Preservation of anomalously high porosity in deeply buried sandstones by grain-coating chlorite: examples from the Norwegian continental shelf. AAPG (Am. Assoc. Pet. Geol.) Bull. 77 (7), 1260–1286.

Ercegovac, M., Kostic, A., 2006. Organic facies and palynofacies: nomenclature, classification and applicability for petroleum source rock evaluation. Coal Geol. 68, 70–78.

Espitalié, J., Deroo, G., Marquis, F., 1985. La pyrolyse Rock-Eval et ses applications; première partie. Rev. Inst. Fr. Petrol 40, 563–579. https://doi.org/10.2516/ogst:1985035.

Evamy, B.D., 1963. The application of a chemical staining technique to a study of dedolomitisation. Sedimentology 2, 164–170. https://doi.org/10.1111/j.1365-3091.1963.tb01210.x.

Fantasia, A., Föllmi, K.B., Adatte, T., Bernárdez, E., Spangenberg, J.E., Mattioli, E., 2018. The toarcian oceanic anoxic event in southwestern gondwana: an example from the Andean basin, northern Chile. J. Geol. Soc. London. 175, 883–902. https://doi.org/10.1144/jgs2018-008.

Fantin, M., Crousse, L., Cuervo, S., Vallejo, D., Gonzalez Tomassini, F., Reijenstein, H., Lipinsky, C., 2014. Vaca Muerta stratigraphy in central Neuquén Basin: impact on emergent unconventional Project. In: Unconventional Resources Technology Conference, URTeC, 1923793.

Föllmi, K.B., 1995. 160 My record of marine sedimentary phosphorus burial: coupling of climate and continental weathering under greenhouse and icehouse conditions. Geology 23, 503–506. https://doi.org/10.1130/0091-7613(1995)023<0503:MYROMS>2.3.CO;2.

Föllmi, K.B., 1996. The phosphorus cycle, phosphogenesis and marine phosphate-rich deposits. Earth Sci. Rev. 40, 55–124. https://doi.org/10.1016/0012-8252(95)00049-6.

Gautier, D.L., Clayton, J.L., Leventhal, J.S., Reddin, N.J., 1984. Origin and source rock potential of the sharon springs member of the pierre shale, Colorado and Kansas. In: Woodward, J., Meissner, F.F., Clayton, J.L. (Eds.), Source Rocks of the Rocky Mountains: Rocky Mountain Association of Geologists, pp. 369–385.

Gómez Dacal, A.R., Gómez Peral, L.E., Spalletti, L.A., Sial, A.N., Siccardi, A., Poiré, D.G., 2018. First record of the Valanginian positive carbon isotope anomaly in the Mendoza shelf, Neuquén Basin, Argentina: palaeoclimatic implications. Andean Geol. 45, 111–129. https://doi.org/10.5027/andgeov45n2-3059.

González, G., Jait, D., Benoit, S., Sylwan, C., 2016. Capítulo 5: lindero atravesado. In: González, G., Vallejo, M.D., Kietzmann, D., Marchal, D., Desjardins, P., González Tomassini, F., Gómez Rivarola, L., Domínguez, R.F., Fantin, M. (Eds.), Regional Cross Section of the Vaca Muerta Formation Integration of Seismic, Well Logs, Cores and Outcrops. Instituto Argentino del Gas y Petróleo, Buenos Aires, pp. 45–58.

Götz, A., Szule, J., Feist-Burkhardt, S., 2005. Distribution of sedimentary organic matter in Anisian carbonate series of S Poland: evidence of third-order sea-level fluctuations. Int. J. Earth Sci. 94, 267–274. https://doi.org/10.1007/s00531-005-0469-0.

Gulisano, C.A., 1981. El ciclo Cuyano en el norte de Neuquén y sur de Mendoza. VIII Congreso Geológico Argentino-Buenos Aires Actas 3, 572–592.

Hallam, A., 1984. Continental humid and arid zones during the Jurassic and Cretaceous. Palaeogeogr. Palaeoclimatol. Palaeoecol. 47, 195–223. https://doi.org/10.1016/0031-0182(84)90094-4.

Hallock, P., Schlager, W., 1986. Nutrient excess and the demise of coral reefs and carbonate platforms. Palaios 1, 389–398. https://doi.org/10.2307/3514476.

Hesselbo, S., Deconinck, J., Hugget, J., Morgans-Bell, H., 2009. Jurassic paleoclimatic change from clay mineralogy and gamma-ray spectrometry of the Kimmeridge Clay, Dorset, UK. J. Geol. Soc. 166, 1123–1133. https://doi.org/10.1144/0016-76492009-070. London.

Hillier, S., 1995. Erosion, sedimentation and sedimentary origin of clays. In: Velde, B. (Ed.), Origin and Mineralogy of Clays. Springer-Verlag Berling Heidelberg, pp. 162–219. https://doi.org/10.1007/978-3-662-12648-6.

Hillier, S., Wilson, M.J., Merriman, R.J., 2006. Clay mineralogy of the old red sandstone and devonian sedimentary rocks of wales, scotland and england. Clay Miner. 41, 433–471. https://doi.org/10.1180/0009855064110203.

Huggett, J., Burley, S., Longstaffe, F., Saha, S., Oates, M., 2015. The nature and origin of authigenic chlorite and related cements in oligo-miocene reservoir sandstones, Tapti gas fields, Surat depression, offshore western India. J. Petrol. Geol. 38 (4), 383–410.

Howell, J.A., Schwarz, E., Spalletti, L.A., Veiga, G.D., 2005. The Neuquén basin: an overview. In: Veiga, G.D., Spalletti, L.A., Howell, J.A., Schwarz, E. (Eds.), The Neuquén Basin, Argentina: A Case Study in Sequence Stratigraphy and Basin Dynamics, vol. 252. Geological Society of London, Special Publications, pp. 1–14.

Hower, J., Eslinger, E.V., Hower, M.E., Perry, E.A., 1976. Mechanism of burial metamorphism of argillaceous sediment. Geol. Soc. Am. Bull. 87, 725–737. https://doi.org/10.1130/0016-7606(1976)87<725.

Iijima, A., 1988. Diagenetic transformation of minerals as exemplified by zeolites and silica minerals—a Japanese view. In: Chilingarian, G.V., y K, H., Wolf, K.H. (Eds.), Diagenesis II, Developments in Sedimentology, vol. 43. Elsevier Science Publishers, Amsterdam, pp. 147–211.

International Atomic Energy Agency, 2003. Guidelines for Radioelement Mapping Using Gamma Ray Spectrometry Data, p. 173. Vienna.

Jarvie, D.M., Hill, R.J., Ruble, T.E., Pollastro, R.M., 2007. Unconventional shale-gas systems: the Mississippian Barnett Shale of north-central Texas as one model for thermogenic shale-gas assessment. Am. Assoc. Petrol. Geol. Bull. 91, 475–499. https://doi.org/10.1306/12190606068.

Katz, M.E., Wright, T.J., Miller, K.G., Cramer, B.S., Fennel, K., Falkowski, P.G., 2005. Biological overprint of the geological carbon cycle. Mar. Geol. 214, 323–338. https://doi.org/10.1016/j.margeo.2004.08.005.

Kietzmann, D.A., Palma, R.M., Riccardi, A.C., Martín-Chivelet, J., López-Gómez, J., 2014. Sedimentology and sequence stratigraphy of a Tithonian-Valanginian carbonate ramp (Vaca Muerta Formation): a misunderstood exceptional source rock in the Southern Mendoza area of the Neuquén Basin. Argentina. Sediment. Geol. 302, 64–86. https://doi.org/10.1016/j.sedgeo.2014.01.002.

Kietzmann, D.A., Palma, R.M., Iglesia Llanos, M., 2015. Cyclostratigraphy no fan orbitally-driven Tithonian-Valanginian carbonate ramp succession, Soutehrn Mendoza, Argentina: implications for the Jurassic-Cretaceous boundary in the Neuquén Basin. Sediment. Geol. 315, 29–46. https://doi.org/10.1016/j.sedgeo.2014.10.002.

Kietzmann, D.A., Ambrosio, A.L., Suriano, J., Alonso, M.S., Tomassini, F.G., Depine, G., Repol, D., 2016. The vaca muerta-quintuco system (Tithonian-Valanginian) in the Neuquén Basin, Argentina: a view from the outcrops in the Chos malal fold and thrust belt. Am. Assoc. Petrol. Geol. Bull. 100, 743–771. https://doi.org/10.1306/02101615121.

Kietzmann, D.A., Ambrosio, A.L., Alonso, M.S., Suriano, J., 2018a. Chapter 20: Puerta Curaco. In: González, G., Vallejo, M.D., Kietzmann, D., Marchal, D., Desjardins, P., González Tomassini, F., Gómez Rivarola, L., Domínguez, R.F., Fantin, M. (Eds.), Regional Cross Section of the Vaca Muerta Formation Integration of Seismic, Well Logs, Cores and Outcrops. Instituto Argentino del Gas y Petróleo, Buenos Aires, pp. 219–232.

Kietzmann, D.A., Iglesia-Llanos, M.P., Kohan Martinez, M., 2018b. Astronomical calibration of the upper jurassic-lower cretaceous in the Neuquén Basin, Argentina: a contribution from the southern hemisphere to the geologic time scale. In: Montenari, M. (Ed.), Stratigraphy & Timescales 3. Elsevier, Amsterdam, pp. 328–355. https://doi.org/10.1016/bs.sats.2018.07.003.

Kietzmann, D.A., Gonzalez Tomassini, F., Smith, T., 2020. Grain association, petrography, and lithofacies. In: Minisini, D., Fantin, M., Lanusse Noguera, I., y Leanza, H.A. (Eds.), Integrated Geology of Unconventionals: the Case of the Vaca Muerta Play, Argentina, vol. 121. American Association of Petroleum Geologists, Memoir, pp. 267–296. https://doi.org/10.1306/13682230M1203829.

Kietzmann, D.A., Llanos, M.P.I., Tomassini, F.G., Noguera, I.L., Vallejo, D., Reijenstein, H., 2021a. Upper jurassic–lower cretaceous calpionellid zones in the Neuquén Basin (southern andes, Argentina): correlation with ammonite zones and biostratigraphic synthesis. Cretac. Res. 127 https://doi.org/10.1016/j.cretres.2021.104950.

Kietzmann, D.A., Iglesia Llanos, M.P., Palacio, J.P., Sturlesi, M.A., 2021b. Facies analysis and stratigraphy throughout the jurassic-cretaceous boundary in a new basinal tithonian–berriasian section of the vaca Muerta Formation, las tapaderas, southern Mendoza andes, Argentina. J. S. Am. Earth Sci. 109, 103267.

Kietzmann, D.A., Iglesia Llanos, M.P., Iovino, F., 2023. Tithonian–Berriasian calcisphere (calcareous dinoflagellate cysts) zones in the Neuquén Basin, Argentina: correlation between Southern Andes and Tethyan regions. Newsl. Stratigr. 56 (2) (in press).

Kohan Martinez, M., 2022. Magnetoestratigraffía y cicloestratigrafía de magnetismo de rocas de la Formación Vaca Muerta (Jurásico Superior - Cretácico Inferior), Cuenca Neuquina. Universidad de Buenos Aires, Buenos Aires, p. 333. PhD Thesis.

Krim, N., Bonnel, C., Tribovillard, N., Imbert, P., Aubourg, C., Riboulleau, A., Bout-Roumazeilles, V., Hoareau, G., Fasentieux, B., 2017. Paleoenvironmental evolution of the southern neuquèn basin (Argentina) during the tithonian-berriasian (vaca muerta and picún leufú formations): a multi-proxy approach. Bull. la Société géologique Fr. 188, 34. https://doi.org/10.1051/bsgf/2017196.

Krim, N., Tribovillard, N., Riboulleau, A., Bout-Roumazeilles, V., Bonnel, C., Imbert, P., Aubourg, C., Hoareau, G., Fasentieux, B., 2019. Reconstruction of palaeoenvironmental conditions of the Vaca Muerta formation in the southern part of the Neuquén Basin (Tithonian-Valanginian): evidences of initial short-lived development of anoxia. Mar. Petrol. Geol. 103, 176–201. https://doi.org/10.1016/j.marpetgeo.2019.02.011.

Kübler, B., 1987. Cristallinité d l' illite, méthodes normalisées de préparations de mesure, méthodes normalisées de mesures. In: Neuchâtel, Suisse, vol. 1. Cahiers Institut Géologie série ADX, pp. 1–13.

Land, L.S., Milliken, K.L., 1981. Feldspar diagenesis in the frio formation, brazoria county, Texas gulf coast. Geology 9, 314–318. https://doi.org/10.1130/0091-7613(1981)9<314:FDITFF>2.0.CO;2.

Lanusse Noguera, I., Fantin, M.A., Crespo, P.A., Crousse, L.C., Reijenstein, H., Varela, R. A., Bonelli, A., Morales, F., 2017. Multi-disciplinary approach for a landing point criteria in vaca muerta formation. In: SPE/AAPG/SEG Unconventional Resources Technology Conference 2017. https://doi.org/10.15530/urtec-2017-2670565.

Lanz, M., Azmy, K., Cesaretti, N., Fortunatti, N., 2021. Diagenesis of the vaca Muerta Formation Neuquén Basin: evidence from petrography, microthermometry and geochemistry. Mar. Petrol. Geol. 124, 104769 https://doi.org/10.1016/j.marpetgeo.2020.104769.

Leanza, H.A., Hugo, C.A., 1977. Sucesión de amonites y edad de la Formación Vaca Muerta y sincrónicas entre los Paralelos 35°y 40° l.s. Cuenca Neuquina-Mendocina. Rev. Asoc. Geol. Argent. 32, 248–264.

Legarreta, P.N., 2009. Formacion Milichinco en el perfil Puerta Curaco: secuencias, facies y evolución paleoambiental. Cuenca Neuquina, provincia del Neuquén, Argentina. Trabajo Final de Licenciatura, Universidad de Buenos Aires (inédito), Buenos Aires, p. 200.

Legarreta, L., Gulisano, C.A., 1989. Análisis estratigráfico secuencial de la Cuenca neuquina (triásico superior-terciario inferior, Argentina). In: En, Chebli, G.A., Spalletti, L.A. (Eds.), Cuencas Sedimentarias Argentinas, Simposio de Cuencas Sedimentarias Argentinas, 10°. Congreso Geológico Argentino, Tucumán, pp. 221–243.

Legarreta, L., Uliana, M.A., 1991. Jurassic-Cretaceous marine oscillations and geometry of back arc basin, central Argentina andes. In: McDonald, D. (Ed.), Sea Level Changes at Active Plate Margins: Process and Product, vol. 12. International Association of Sedimentologists Special Publication, Oxford, pp. 429–450.

Legarreta, L., Villar, H.J., 2015. Vaca Muerta Formation (late jurassic - early cretaceous): sequences, facies and source rock characteristics. In: 3rd Unconv. Resour. Technol. Conf. San Antonio, p. 15. https://doi.org/10.15530/urtec-2015-2170906.

Lerouge, C., Gaucher, E., Tournassat, C., Négrel, P., Crouzet, C., Guerrot, C., Gautier, A., Michel, P., Vinsot, A., Buschaert, S., 2010. Strontium distribution and origins in a natural clayey formation (Callovian-Oxfordian, Paris Basin, France): a new sequential extraction procedure. Geochmica et Cosmochimica Acta 2926–2942. https://doi.org/10.1016/j.gca.2010.02.013.

Liu, B., Schieber, J., Mastalerz, M., Teng, J., 2020. Variability of rock mechanical properties in the sequence stratigraphic context of the upper devonian new albany shale, Illinois basin. Mar. Petrol. Geol. 112, 104068 https://doi.org/10.1016/j.marpetgeo.2019.104068.

McArthur, J.M., 2019. Early Toarcian black shales: a response to an oceanic anoxic event or anoxia in marginal basins? Chem. Geol. 522, 71–83. https://doi.org/10.1016/j.chemgeo.2019.05.028.

Mendonça Filho, J.G., Rêgo Menezes, T., Oliveira Mendonça, J., Donizeti de Oliveira, A., Freitas da Silva, T., Franco Rondon, N., Sobrinho da Silva, F., 2012. Organic facies: palynofacies and organic geochemistry approaches. In: Dionisios Panagiotaras, Dr (Ed.), Geochemistry - Earth's System Processes. InTech, 978-953-51-0586-2.

Micucci, E., Bande, A., Starck, D., Veiga, R., 2018. El Jurásico del Dorso de los Chihuidos, contribución a su conocimiento. X Congreso de Exploración y Desarrollo de Hidrocarburos, Argentina, pp. 437–460.

Milliken, K.L., Olson, T., 2017. Silica diagenesis, porosity evolution, and mechanical behavior in, siliceous mudstones, Mowry shale (Cretaceous), Rocky Mountains, U.S. A. J. Sediment. Res. 87, 366–387. https://doi.org/10.2110/jsr.2017.24.

Milliken, K.L., Reed, R.M., McCarty, D.K., Bishop, J., Lipinski, C.J., Fischer, T.B., Crousse, L., Reijenstein, H., 2019. Grain assemblages and diagenesis in the Vaca Muerta Formation (Jurassic-Cretaceous), Neuquén Basin, Argentina. Sediment. Geol. 380, 45–64. https://doi.org/10.1016/j.sedgeo.2018.11.007.

Minisini, D., Fryklund, B., Gerali, F., Fantin, M., 2020a. The First Economical Unconventional Play outside North America: Context, History, and "Coopetition". In: Minisini, D., Fantin, M., Lanusse Noguera, I., Leanza, H. (Eds.), Integrated Geology of Unconventionals: the Case of the Vaca Muerta Play, Argentina, vol. 121. AAPG Memoir, pp. 1–24. https://doi.org/10.1306/13682221M1203264.

Minisini, D., Desjardins, P., Otharán, G., Paz, M., Kietzmann, D., Eberli, G., Zavaloa, C., Simo, T., Macquaker, J., Heine, C., 2020b. Sedimentology, depositional model, and implications ofr reservoir quality. In: Minisini, D., Fantin, M., Lanusse Noguera, I., Leanza, H. (Eds.), Integrated Geology of Unconventionals: the Case of the Vaca Muerta Play, Argentina, vol. 121. AAPG Memoir, pp. 201–236. https://doi.org/10.1306/13682228M1203264.

Mitchum, R.M., Uliana, A., 1985. Seismic stratigraphy of carbonate depositional sequences, Upper Jurassic-Lower Cretaceous. Neuquén Basin, Argentina. In: Berg, R. B., Wollverton, D.G. (Eds.), Seismic Stratigraphy: an Integrated Approach to Hydrocarbon Exploration, vol. 39. AAPG Memoir, pp. 255–274.

Moore, D.M., Reynolds, R.C., 1997. X-Ray Diffraction and the Identification and Analysis of Clay Minerals. Oxford University Press, New York, USA, p. 379.

Morales, C., Gardin, S., Schnyder, J., Spangenberg, J., Arnaud-Vanneau, A., Arnaud, H., Adatte, T., Föllmi, K.B., 2013. Berriasian and early Valanginian environmental change along a transect from the Jura Platform to the Vocontian Basin. Sedimentology 60, 36–63. https://doi.org/10.1111/sed.12019.

Morales, C., Spangenberg, J., Arnaud-Vanneau, A., Adatte, T., Föllmi, K., 2016. Evolution of the northern Tethyan Helvetic Platform during the late Berriasian and Early Valanginian. The depositional Record 2 (1), 47–73. https://doi.org/10.1002/dep2.13.

Musacchio, J., Bande, A., Capelli, I., Scasso, R., 2022. Análisis geoquímico con énfasis en el contenido de fósforo del Sistema Vaca Muerta-Quintuco en el sector central de la Cuenca Neuquina. XI Congreso de Exploración y Desarrollo de Hidrocarburos, Argentina, pp. 17–31.

Ortiz, A., Crousse, L., Bernhardt, C., Vallejo, D., Mosse, L., 2020. Reservoir properties: mineralogy, porosity, and fluid types. In: Minisini, D., Fantin, M., Lanusse Noguera, I., Leanza, H. (Eds.), Integrated Geology of Unconventionals: the Case of the Vaca Muerta Play, Argentina, vol. 121. AAPG Memoir, pp. 329–350. https://doi.org/10.1306/13682232M1203835.

Otharán, G., Zavala, C., Arcuri, M., Di Meglio, M., Zorzano, A., Marchal, D., Köhler, G., 2020. Análisis de facies de fangolitas bituminosas asociadas a flujos fluios de fango. Sección Inferior de la Formación Vaca Muerta (Tithoniano), Cuenca Neuquina central, Argentina. Andean Geol. 47, 384–417.

Otharán, G., Zavala, C., Schieber, J., Olivera, D., Martínez, M., Díaz, P., Yawar, Z., Agüero, L., 2022. Uneavelling the fabrics preserved inside early diagenetic concretions: Insights for the distribution, accumulation and preservation of organic-rich mud in the interior of epicontinental basins. Sediment. Geol. 440, 106254 https://doi.org/10.1016/j.sedgeo.2022.106254.

Paz, M., Ponce, J., Mángano, M.G., Buatois, L.A., Carmona, N.B., Wetzel, A., Pereira, E., Rodríguez, M.N., 2021. The Vaca Muerta transgression (Upper Jusassic), Neuquén Basin, Argentina: Insights into the evolution and timing of aeolian-marine transitions. Sedimentology 68, 2732–2764.

Paz, M., Buatois, L., Mángano, M.G., Desjardins, P., Notta, A., González Tomassini, F., Carmona, N., Minisini, D., 2022. Organic-rich, fine-grained contourites in an epicontinental basin: The Upper Jurassic-Lower Cretaceous Vaca Muerta Formation, Argentina. Mar. Petrol. Geol. 142, 105757 https://doi.org/10.1016/j.marpetgeo.2022.105757.

Paz, M., Mángano, M.G., Buatois, L.A., Desjardins, P.R., Minisini, D., González Tomassini, F., Rodríguez, M.N., Pereira, E., Fantín, M., Parada, M.N., Carmona, N.B., 2023. Environmental control son trace-fossil distribution in the Upper Jurassic-Lower Cretaceous Vaca Muerta Formation (Argentina): Implications for the analysis of the fine-grained depositional systems. Sediment. Geol. 454, 106460.

Pedersen, T.F., Calvert, S.E., 1990. Anoxia vs. productivity: what controls the formation of organic- carbon-rich sediments and sedimentary rocks? Am. Assoc. Petrol. Geol.

Bull. 74, 454–466. https://doi.org/10.1306/0C9B232B-1710-11D7-8645000102C1865D.
Peltonen, C., Marcussen, O., Bjørlykke, K., Jahren, J., 2009. Clay mineral diagenesis and quartz cementation in mudstones: the effects of smectite to illite reaction on rock properties. Mar. Petrol. Geol. 26, 887–898. https://doi.org/10.1016/j.marpetgeo.2008.01.021.
Peters, K., Cassa, M., 1994. Applied Source Rock Geochemistry. In: Magoon, L., Dow, W. (Eds.), The Petroleum System-From Source to Trap AAPG Memoir 60, pp. 93–120.
Piper, D.Z., Calvert, S.E., 2009. A marine biogeochemical perspective on black shale deposition. Earth Sci. Rev. 95, 63–96. https://doi.org/10.1016/j.earscirev.2009.03.001.
Ponce, C., Alvarez, L., Martínez Lampe, J., 2022. Expandiendo los límites de la Formación aca Muerta en área de alto riesgo exploratorio Chihuido de la Sierra Negra. XI Congreso de Exploración y Desarrollo de Hidrocarburos, Argentina, pp. 163–171.
Ramos, V.A., 1999. Evolución Tectónica de la Argentina. In: Caminos, R. (Ed.), Geología Argentina, vol. 29. Instituto de Geología y Recursos Minerales, Anales, pp. 715–759.
Ravier, E., Martinez, M., Pellenard, P., Zanella, A., Tupinier, L., 2020. The Milankovitch fingerprint on the distribution and thickness of bedding-parallel veins (beef) in source rocks. Mar. Petrol. Geol. 122 https://doi.org/10.1016/j.marpetgeo.2020.104643.
Reijenstein, H.M., Posamentier, H.W., Bande, A., Lozano, F.A., Domínguez, R.F., Wilson, R., Catuneanu, O., Galeazzi, S., 2020. Seismic geomorphology, depositional elements, and clinoform sedimentary processes: impact on unconventional reservoir prediction. In: Minisini, D., Fantin, M., Lanusse Noguera, I., Leanza, H. (Eds.), Integrated Geology of Unconventionals: the Case of the Vaca Muerta Play, Argentina, vol. 121. AAPG Memoir, pp. 237–266. https://doi.org/10.1306/13682221M1203264.
Révész, K.M., Landwehr, J.M., 2002. δ13C and δ18O isotopic composition of CaCo3 measured by continuous flow isotope ratio mass spectrometry: Statistical evaluation and verification by application to Devils Hole core DH-11 calcite. Rapid Commun. Mass Spectrom. 16, 2102–2114. https://doi.org/10.1002/rcm.833.
Rickman, R., Mullen, M., Petre, E., Grieser, B., Kundert, D., 2008. A Practical Use of Shale Petrophysics for Stimulation Design Optimization: All Shale Plays Are Not Clones of the Barnet Shale. SPE115258, pp. 1–11.
Rietveld, H.M., 1969. A profile refinement method for nuclear and magnetic structures. J. Appl. Crystallogr. 2, 65–71. https://doi.org/10.1107/s0021889869006558.
Rodriguez Blanco, L., Eberli, G., Swart, P., Weger, R., Tenaglia, M., 2018. Stable Isotope Signature of the Tithonian-Valanginian Strata of the Vaca Muerta-Quintuco System in the Neuquén Basin. X Congreso de Exploración y Desarrollo de Hidrocarburos, Argentina, pp. 43–59.
Rodriguez Blanco, L., Eberli, G., Weger, R., Swart, P., Tenaglia, M., Rueda Sanchez, L., McNeill, D., 2020. Periplatform ooze in a mixed siliciclastic-carbonate system – Vaca Muerta Formation, Argentina. Sediment. Geol. 396 https://doi.org/10.1016/j.sedgeo.2019.105521.
Rodriguez Blanco, L., Swart, P., Eberli, G., Weger, R., 2022a. Negative δ13Ccarb values at the Jurassic-Cretaceous boundary – Vaca Muerta Formation, Neuquén Basin, Argentina. Palaeogeography, Palaeoclimatology, Palaeoecology 603, 111208. https://doi.org/10.1016/j.palaeo.2022.111208.
Rodriguez Blanco, L., Eberli, G., Weger, R., McNeill, D., Swart, P., 2022b. Quantifying concretion distribution in shales of the Vaca Muerta-Quintuco system, Neuquén Basin, Argentina. Am. Assoc. Petrol. Geol. Bull. 106 (2), 409–436. https://doi.org/10.1306/08182120059.
Rosemblat, A., Lanusse Noguera, I., Domínguez, F., Guerberoff, D., 2016. Capítulo 12 : Bajada de Añelo. In: González, G., Vallejo, M.D., Kietzmann, D., Marchal, D., Desjardins, P., González Tomassini, F., Gómez Rivarola, L., Domínguez, R.F., Fantin, M. (Eds.), Regional Cross Section of the Vaca Muerta Formation Integration of Seismic, Well Logs, Cores and Outcrops. Instituto Argentino del Gas y Petróleo, Buenos Aires, pp. 131–142.
Ross, D.J.K., Bustin, R.M., 2009. Investigating the use of sedimentary geochemical proxies for paleoenvironment interpretation of thermally mature organic-rich strata: Examples from the Devonian-Mississippian shales, Western Canadian Sedimentary Basin. Chem. Geol. 260, 1–19. https://doi.org/10.1016/j.chemgeo.2008.10.027.
Rutman, P., Hoareau, G., Kluska, J., Lejay, A., Fialips, C., Gelin, F., Aubourg, C., Hernandez Bilbao, E., 2021. Diagenesis and alteration of subsurface volcanic ash beds of the Vaca Muerta Formation, Argentina. Mar. Petrol. Geol. 132, 105220.
Rybacki, E., Meier, T., Dresen, G., 2016. What controls the mechanical properties of shale rocks? - Part II: Brittleness. J. Pet. Sci. Eng. 144, 39–58. https://doi.org/10.1016/j.petrol.2016.02.022.
Saelen, G., Tyson, R. v, Telnaes, N., Talbot, M.R., 2000. Contrasting watermass conditions during deposition of the Whitby Mudstone (Lower Jurassic) and Kimmeridge Clay (Upper Jurassic) formations, UK. Palaeogeogr. Palaeoclimatol. Palaeoecol. 163, 163–196.
Scasso, R.A., Alonso, M.S., Lanés, S., Villar, H.J., Lippai, H., 2002. Petrología y geoquímica de una ritmita marga-caliza del Hemisferio Austral: El Miembro Los Catutos (Formación Vaca Muerta, Tithoniano medio de la Cuenca Neuquina. Rev. la Asoc. Geol. Argentina 57, 143–159.
Scasso, R.A., Alonso, M.S., Lanés, S., Villar, H.J., Laffitte, G., 2005. Geochemistry and petrology of a Middle Tithonian limestone-marl rhythmite in the Neuquén Basin, Argentina: Depositional and burial history. In: Veiga, G.D., Spalletti, L.A., Howell, J. A., Schwarz, E. (Eds.), The Neuquén Basin, Argentina: A Case Study in Sequence Stratigraphy and Basin Dynamics, vol. 252. Geological Society of London, Special Publications, pp. 207–229. https://doi.org/10.1144/GSL.SP.2005.252.01.10.
Schnyder, J., Gorin, G., Soussi, M., Baudin, F., Deconinck, J.F., 2005. Enregistrement de la variation climatique au passage Jurassique/Crétacé' sur la marge sud de la Téthys: minéralogie des argiles et palynofacies de la coupe du Jebel Meloussi (Tunisie Centrale, Formation Sidi Kralif). Bull. Soc. Geol. Fr. 176 (2), 171–182.
Schnyder, J., Ruffell, A., Deconinck, J.F., Baudin, F., 2006. Conjunctive use of spectral gamma-ray logs and clay mineralogy in defining late Jurassic-early Cretaceous palaeoclimate change (Dorset, U.K.). Palaeogeogr. Palaeoclimatol. Palaeoecol. 229, 303–320. https://doi.org/10.1016/j.palaeo.2005.06.027.
Spacapan, J.B., Comerio, M., Brisson, I., Rocha, E., Cipollone, M., Hidalgo, J.C., 2021. Integrated source rock evaluation along the maturation gradient. Application to the Vaca Muerta Formation, Neuquén Basin of Argentina. Basin Res. 1–29 https://doi.org/10.1111/bre.12599.
Spalletti, L.A., Franzese, J.R., Matheos, S.D., Schwarz, E., 2000. Sequence stratigraphy of a tidally dominated carbonate-siliciclastic ramp; the Tithonian-Early Berriasian of the southern Neuquén Basin, Argentina. J. Geol. Soc. London. 157, 433–446. https://doi.org/10.1144/jgs.157.2.433.
Spalletti, L.A., Schwarz, E., Veiga, G.D., 2014. Geoquímica inorgánica como indicador de procedencia y ambiente sedimentario en sucesiones de lutitas negras: Los depósitos transgresivos titonianos (formación Vaca Muerta) de la Cuenca Neuquina, Argentina. Andean Geol. 41, 401–435. https://doi.org/10.5027/andgeoV41n2-a07.
Spalletti, L.A., Pirrie, D., Veiga, G.D., Schwarz, E., Rollinson, G., Shail, R., Haberlah, D., Butcher, A., 2015. Análisis mineralógico integrado (QEMSCAN y DRX) de lutitas negras: los depósitos tithonianos basales de la Formación Vaca Muerta (Cuenca Neuquina, Argentina). Lat. Am. J. Sedimentol. Basin Anal. 22 (1), 13–28.
Spalletti, L.A., Remírez, M.N., Sagasti, G., 2019. Geochemistry of aggradational - Progradational sequence sets of the Upper Jurassic – Lower Cretaceous Vaca Muerta shales (Añelo area, Neuquén Basin, Argentina): Relation to changes in accommodation and marine anoxia. J. South Am. Earth Sci. 93, 495–509. https://doi.org/10.1016/j.jsames.2019.02.011.
Spangenberg, J.E., Zufferey, V., 2019. Carbon isotope compositions of whole wine, wine solid residue, and wine ethanol, determined by EA/IRMS and GC/C/IRMS, can record the vine water status-a comparative reappraisal. Anal. Bioanal. Chem. 41, 2031–2043.
Spangenberg, J.E., Jacomet, S., Schibler, J., 2006. Chemical analyses of organic residues in archaeological pottery from Arbon Bleiche 3, Switzerland - evidence for dairying in the late Neolithic. J. Archaeol. Sci. 33, 1–13.
Steffen, D., Gorin, G.E., 1993. Palynofacies of the Upper Tithonian-Berriasian deepsea carbonates in the Vocontian Trough (SE France). Centres Recherches Exploration-Production Elf-Aquitaine, Bulletin 17, 235–247.
Stein, R., 1986. Organic carbon and sedimentation rate – further evidence for anoxic deep-water conditions in the Cenomanian/Turonian Atlantic Ocean. Mar. Geol. 72, 199–209.
Stinco, L., Barredo, S., 2014. Vaca Muerta formation: An example of shale heterogeneities controlling hydrocarbon's accumulations. In: Soc. Pet. Eng. - SPE/AAPG/SEG Unconv. Resour. Technol. Conf, vol. 2, pp. 2854–2868. https://doi.org/10.15530/urtec-2014-1922563.
Summerhayes, C.P., 1987. Organic-rich Cretaceous sediments from the North Atlantic. In: Brooks, J., Fleet, A.J. (Eds.), Marine Petroleum Source Rocks, vol. 26. Geological Society Special Publication, pp. 301–316.
Tenaglia, M., Eberli, G., Weger, R., Rodriguez Blanco, L., Rueda, L., Swart, P., 2020. Total organic carbon quantification from wireline logging techniques: a case study in the Vaca Muerta Formation, Argentina. J. Petrol. Sci. Eng. 194, 107489 https://doi.org/10.1016/j.petrol.2020.107489.
Theng, B.K., 1979. Formation and Properties of Clay-Polymer Complexes. Elsevier Stienfic Publishin Company, p. 362.
Tissot, B.P., Welte, D.H., 1984. Petroleum Formation and Occurrence. Springer-Verlag Berlin Heidelgerg, New York Tokyo, p. 699.
Tribovillard, N., Algeo, T.J., Lyons, T., Riboulleau, A., 2006. Trace metals as paleoredox and paleoproductivity proxies: An update. Chem. Geol. 232, 12–32. https://doi.org/10.1016/j.chemgeo.2006.02.012.
Tyson, R.V., 1989. Late Jurassic palynofacies trends, Piper and Kimmeridge Clay formations, UK onshore and offshore. In: Batten, D.J., Keen, M.C. (Eds.), Northwest European Micropalaeontology and Palynology. British Micropalaeontological Society Series, Chichester, pp. 135–172.
Tyson, R.V., 1993. Palynofacies analysis. In: Jenkins, D.J. (Ed.), Applied Micropalaeontology. Kluwer, Dordrecht, pp. 153–191.
Tyson, R.V., 1995. Sedimentary Organic Matter; Organic Facies and Palynofacies. Chapman and Hall, London, p. 615.
Uliana, M.A., Legarreta, L., 1993. Hydrocarbons habitat in a triassic-to-cretaceous sub-andean setting: Neuquén basin, Argentina. J. Petrol. Geol. 16, 397–420. https://doi.org/10.1111/j.1747-5457.1993.tb00350.x.
Utada, M., 2001. In: Bish, D.L., Ming, D.W. (Eds.), Natural Zeolites: Occurrence, Properties, Applications, Mineralogical Society of America Reviews in Mineralogy and Geochemestry, vol. 45, pp. 277–300.
Varela, R., Marchal, D., Cuervo, S., Lombardo, E., Perl, Y., Hryb, D., Pateti, P., Nielsen, O., 2020. Geomechanics: Pressure, Stress Field, and Hydraulic fractures. In: Minisini, D., Fantin, M., Lanusse Noguera, I., Leanza, H. (Eds.), Integrated Geology of Unconventionals: the Case of the Vaca Muerta Play, Argentina, vol. 121. AAPG Memoir, pp. 351–376. https://doi.org/10.1306/13682233M1203836.
Veiga, R., Bande, A., Micucci, E., Mosquera, A., Macellari, C., 2018. Análisis en la capacidad de almacenamiento de gas a partir del uso de registros de pozo. Ejemplos en la Fm. Vaca Muerta. Petrotecnia 3, 64–84.
Veiga, R., Vergani, G., Brissón, I., Macellari, C., Leanza, H., 2020. The Neuquén Super Basin. Am. Assoc. Petrol. Geol. Bull. 104 (12), 2521–2555. https://doi.org/10.1306/09092020023.
Vergani, G., Tankard, A., Belotti, H., Welsink, H., 1995. Tectonic evolution and paleogeography of the Neuquén basin, Argentina. In: Tankard, A., Suarez, S.,

Welsink, H. (Eds.), Petroleum Bains of South America AAPG Memoir, vol. 62, pp. 383–402.
Volkheimer, W., Melendi, D., 1976. Palinomorfos como fósiles guías (3ra. Parte). Técnicas de laboratorio palinológico. Revista Minera, Geología y Mineralogía. Sociedad Argentina de Minería y Geología 34, 19–30.
Wagreich, M., Koukal, V., 2019. The pelagic archive of short-term sea-level change in the Cretaceous: a review of proxies linked to orbital forcing. In: Wagreich, M., Hart, M., Sames, B., Yilmaz, I. (Eds.), Cretaceous Climate Events and Short-Term Sea-Level Changes, vol. 498. Geological Society, Londo. Special Publication. https://doi.org/10.1144/SP498-2019-34.
Wang, F.P., Gale, J.F.W., 2009. Screening Criteria for Shale-Gas Systems. Gulf Coast Assoc. Geol. Soc. Trans. 59, 779–793, 2009.
Weaver, C.E., 1931. Paleontology of the Jurassic and Cretaceous of West Central Argentina, vol. 1. Memoirs University of Washington, p. 469.
Wedepohl, K.H., 1971. Environmental influences on the chemical composition of shales and clays. In: Ahrens, L.H., Press, F., Runcorn, S.K., Urey, H.C. (Eds.), Physics and Chemistry of the Earth, pp. 307–331.
Weger, R., Eberli, L. Rodriguez Blanco y G., 2017. A basinal reference section and lateral variability of the Vaca Muerta Formation in the Neuquén Basin, Argentina. In: XX Congreso Geológico Argentino- Simposio 5, San Miguel de Tucuman, pp. 179–184.
Weger, R.J., Murray, S.T., McNeill, D.F., Swart, P.K., Eberli, G.P., Rodriguez Blanco, L., Tenaglia, M., Rueda, L.E., 2019. Paleothermometry and distribution of calcite beef in the Vaca Muerta Formation, Neuquén Basin, Argentina. Am. Assoc. Petrol. Geol. Bull. 103, 931–950. https://doi.org/10.1306/10021817384.
Weissert, H., Erba, E., 2004. Volcanism, CO_2 and paleoclimate: a Late Jurassic-Early Cretaceous carbon and oxygen isotope record. J. Geol. Soc. 161, 695–702. https://doi.org/10.1144/0016-764903-087. London.
Wignall, P.B., 1991. Model for transgressive black shales? Geology 19, 167–170.
Wignall, P.B., Myers, K.J., 1988. Interpreting benthic oxygen levels in mudrocks: A new approach. Geology 16, 452–455. https://doi.org/10.1130/0091-7613(1988)016<0452:IBOLIM>2.3.CO;2.
Wilson, M.J., Shaldybin, M.V., Wilson, L., 2016. Clay mineralogy and unconventional hydrocarbon shale reservoirs in the USA. I. Occurrence and interpretation of mixed-layer R3 ordered illite/smectite. Earth Sci. Rev. 158, 31–50. https://doi.org/10.1016/j.earscirev.2016.04.004.
Yi-Kai, G., Zhen-Kui, J., Jian-Hua, Z., Xin, W., Zhen-Peng, Z., Yang, W., 2017. Clay minerals in shales of the Lower Silurian Longmaxi Formation in the Eastern Sichuan Basin, China. Clay Miner. 52 (2), 217–233. https://doi.org/10.1180/claymin.2017.052.2.04.
Zeller, M., Reid, S.B., Eberli, G.P., Weger, R.J., Massaferro, J.L., 2015. Sequence architecture and heterogeneities of a field - Scale Vaca Muerta analog (Neuquén Basin, Argentina) - From outcrop to synthetic seismic. Mar. Petrol. Geol. 66, 829–847. https://doi.org/10.1016/j.marpetgeo.2015.07.021.
Zhao, T., Xu, S., Hao, F., 2023. Differential adsorption of clay minerals: Implications for organic matter enrichment. Earth Sci. Rev. 246, 104598.